Influence of a triaxial stress state on the load-deformation behaviour of axisymmetrically corroded reinforcing bars

Author(s):
Haefliger, Severin; Thoma, Karel; Kaufmann, Walter

Publication date:
2023-12-01

Permanent link:
https://doi.org/10.3929/ethz-b-000635383

Originally published in:
Construction and Building Materials 407, https://doi.org/10.1016/j.conbuildmat.2023.132737

Construction and Building Materials 407 (2023) 132737

Contents lists available at ScienceDirect

Construction and Building Materials

journal homepage: www.elsevier.com/locate/conbuildmat

Influence of a triaxial stress state on the load-deformation behaviour of axisymmetrically corroded reinforcing bars

Severin Haefliger *, Karel Thoma, Walter Kaufmann

Institute of Structural Engineering, ETH Zurich, 8093 Zurich, Switzerland

ARTICLE INFO

Keywords:
Reinforcing bars
Pitting
Corrosion
Pit geometry
Triaxial stress state
Strain localisation
Load-deformation behaviour

ABSTRACT

Local corrosion damage reduces the load-bearing capacity of reinforcing bars and, even more severely, their deformation capacity. These effects are mainly attributed to the reduced cross-sectional area and the accompanying strain localisation. However, several experimental studies found an altered load-deformation behaviour of naturally corroded as well as artificially damaged reinforcing bars, including an apparently increased tensile strength, which cannot be explained solely by strain localisation. Accordingly, in an experimental campaign carried out by the authors on locally axisymmetrically damaged reinforcing bars, the observed peak load increased with decreasing damage length, and the deformation capacity was much less impaired than predicted by established strain localisation models. A series of nonlinear FE analyses was carried out to investigate a potential effect of the local stress state in the vicinity of the local corrosion damage. The results indeed revealed a triaxial stress state in this region, caused by the local deviation of the stress trajectories, explaining the experimental observations on a mechanical basis, and indicating a pronounced influence of the triaxial stresses on the uniaxial stress–strain behaviour of the bar in the vicinity of the corrosion pit. A parametric study was conducted to investigate a broader range of corrosion damage geometries and the corresponding triaxial stresses. The results indicate that the transverse stresses strongly affect the apparent uniaxial mechanical steel properties (yield stress, tensile strength, deformation capacity, loss of yield plateau) for short damage lengths typically found for pitting corrosion. A simplified modelling approach is proposed to capture the governing effects on the apparent uniaxial stress–strain curve of locally corroded reinforcing bars.

1. Introduction

Uniform and local corrosion reduce the load-bearing capacity of reinforcing bars and reinforced concrete (RC) structures due to the loss of cross-sectional area. In contrast to uniform corrosion, local corrosion additionally impairs the deformation capacity, as shown in many experimental campaigns on naturally corroded and artificially damaged reinforcing bars [1–11]. Recent studies [1,9,11–13] attributed the reduced ductility to strain localisation, proposing independently similar modelling approaches [11,13]. They introduced a critical cross-section loss beyond which most of the deformation capacity of a reinforcing bar is lost [1,13]. These studies also found that the deformation capacity is reduced disproportionally to the cross-section loss, with one study reporting a drastic reduction of the elongation at ultimate force by more than 80% for a cross-section loss of merely 17% [13].

The reduced deformation capacity of corroded reinforcing bars directly impairs the deformation capacity of the affected RC structure, depending on the variation of the residual cross-sectional area of the bars [12,13]. This is particularly crucial for structural safety assessment strategies applying the lower bound theorem of the plasticity theory, which – though often only implicitly – presumes sufficient deformation capacity. Furthermore, quantifying the residual deformation capacity of corroded structures is essential to successfully apply performance-based assessment strategies, i.e., to compare the deformation capacity of a structure to its deformation demand. Such assessments are typically used for the analysis of plastic load redistributions in statically indeterminate structures (e.g., imposed deformations in multi-span bridges), and where the actions on the structure depend on its deformations (e.g., earth pressure on a retaining wall, seismic loading). Therefore, the mechanical understanding and the accurate modelling of the deformation capacity of corroded reinforcing bars is key for a safe assessment of corroded RC structures.

* Corresponding author.
E-mail addresses: haefliger@ibk.baug.ethz.ch, severin.haefliger@gmx.ch (S. Haefliger).

https://doi.org/10.1016/j.conbuildmat.2023.132737
Received 10 December 2022; Received in revised form 26 May 2023; Accepted 31 July 2023
Available online 30 September 2023

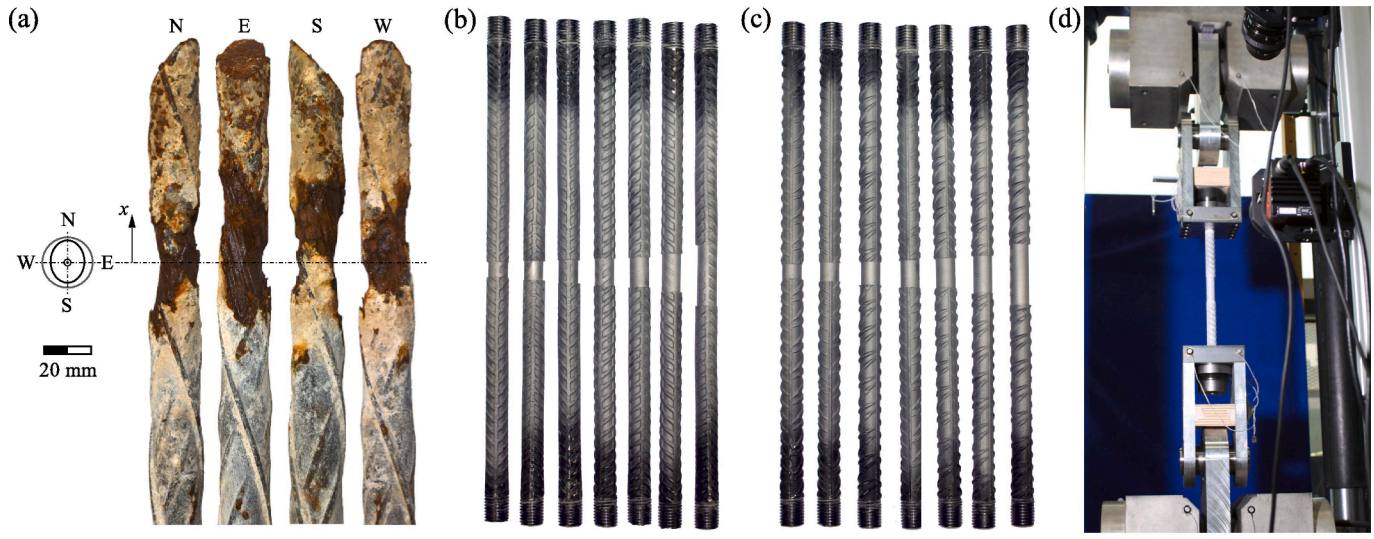

Fig. 1. Example of reinforcing bar with reasonably axisymmetric cross-section loss (a) extracted from an existing cantilever retaining wall [12,36]. Experiments on reinforcing bars with reduced diameter (b-d): Specimens of (b) CW series and (c) QST series after sandblasting; (d) tensile testing machine with spherical hinges and DIC cameras mounted on front side.

1.1. Strain localisation effects

As mentioned above, strain localisation plays a crucial role in the mechanical explanation of the reduced deformation capacity. It can readily be explained by modelling a corroded reinforcing bar as a chain of tension members having different lengths, with equal normal force F but varying tensile stiffness E_sA_s, where E_s = tangent modulus of the reinforcing steel, and A_s = cross-sectional area of the reinforcing bar (reduced by corrosion where applicable). If the tensile stiffness of a member is strongly reduced – which may be caused by severe cross-section loss and/or yielding of the reinforcement – much higher strains $\varepsilon_s = N/E_sA_s$ occur in this weak member than in the remaining members, i.e., the strains localise in the weak member. If this weak member is short, even very high localised strains cause only a small overall elongation (see, e.g., [13]). This typically applies to reinforcing bars affected by severe pitting corrosion, whose cross-section is reduced over a short length. It is particularly pronounced in cases where the tensile strength in the damaged section is reached (i.e., the bar ruptures) while the tensile stress in the regular cross-section is still below the yield stress: substantial deformation occurs only in the short damaged part, and the total elongation of the bar at ultimate load is strongly reduced.

Cross-section loss and damage length are thus decisive parameters regarding strain localisation. For reinforcing bars affected by local corrosion, the extent of strain localisation further depends on the material characteristics of the steel: The ratio of yield stress to tensile strength determines the critical cross-section loss beyond which no plastic strains occur in the undamaged part of the reinforcing bar [1,13]. For smaller cross-section losses, the shape of the steel stress–strain curve, particularly the slope in the strain-hardening phase, is highly relevant as well.

Models based on the strain localisation effect have been developed and successfully applied by [11] to describe the behaviour of corroded bare reinforcing bars, and by [13] to describe the response of concrete tension members containing locally corroded reinforcing bars, accounting for tension stiffening. However, experimental results [1,2,4–6,14] indicate that strain localisation alone cannot explain the observed differences in the load-deformation behaviour of bars with varying pit geometry (pit length and pit shape) but equal cross-section loss.

1.2. Effects beyond strain localisation: Influence of pit geometry

The pit geometry affects (i) the triaxial stress state in the pit region caused by the local deviation of the stress trajectories and, in case of non-axisymmetric corrosion, (ii) local bending moments caused by the shift of the centroidal axis in the pit region.

Triaxial stress states occurring in the vicinity of geometry variations are well investigated in material and mechanical engineering, and their influence on the apparent uniaxial steel characteristics is well-known [15–21]. The occurring stress concentrations can lead to unforeseen failures (especially by fatigue) or undesired plastic deformations in mechanical parts, and considerable efforts have been made to quantify them (see, e.g., [22]). Since the stress concentration and the triaxial stress state strongly depend on the local geometry, closed-form solutions can at most be derived for simple geometries and linear elastic behaviour. For general geometries and nonlinear material behaviour, such as that of steel beyond the yield point, Finite Element analyses are applied nowadays, making use of incremental plasticity models including von Mises' J2-plasticity model and material damage models [19,20]. With such analyses, the effects related to a triaxial stress state can be investigated, ranging from an increase or decrease of the apparent uniaxial yield stress and tensile strength to larger strains at peak stress.

Evidently, these effects are not limited to mechanical parts exhibiting geometrical variations, but equally affect locally damaged reinforcing bars. Indeed, some of the mentioned effects have been observed in experimental campaigns on corroded reinforcing bars: Zhu et al. [4] specifically investigated bars with different pit geometries, reporting significant differences in the stress–strain behaviour among the different geometries despite equal residual cross-sections and, hence, an equal degree of strain localisation. Several studies [1,14,23,24] reported a slight to moderate increase of the apparent uniaxial tensile strength (defined as ultimate load divided by the actual residual cross-sectional area in the damaged zone) with increasing cross-section loss. These observations were either attributed to a variation of material characteristics along the bar, or accounted for by using an average of the reduced and initial cross-sectional areas, but maintaining the nominal uniaxial strength [14]. Only few researchers investigated the triaxial stress state in the vicinity of corrosion pits to date, and to the authors' knowledge, FE analyses investigating the mechanical properties of reinforcing bars containing corrosion pits have only been conducted by [5,25], with [5] pointing out the effect of different pit geometries on the results.

Table 1
Specimen specifications: CW = hot-rolled and cold-worked, QST = hot-rolled, quenched and self-tempered; A_s, $A_{s,c}$ = initial and reduced cross-sectional area obtained from GOM-Scan; ∅, $\varnothing_c$ = initial and reduced diameter; L_c = damage length; ζ = cross-section loss; and $(L_c/2)/\varnothing_c$ = normalised damage length.

Specimen	L_c[mm]	A_s[mm^2]	$A_{s,c}$[mm^2]	∅[mm]	$\varnothing_c$[mm]	ζ[-]	$(L_c/2)/\varnothing_c$[-]
CW-15	15	316.9	278.5	20.09	18.83	0.121	0.40
CW-19	19	316.6	270.7	20.08	18.56	0.145	0.51
CW-23	23	316.3	276.5	20.07	18.76	0.126	0.61
CW-27	27	316.9	279.7	20.09	18.87	0.118	0.72
CW-30	30	317.5	275.4	20.11	18.72	0.133	0.80
CW-38	38	317.5	276.5	20.11	18.76	0.129	1.01
CW-61	61	317.0	274.7	20.09	18.70	0.133	1.63
QST-15	15	329.6	285.7	20.48	19.07	0.133	0.39
QST-19	19	332.0	289.0	20.56	19.18	0.130	0.50
QST-23	23	330.8	289.4	20.52	19.20	0.125	0.60
QST-27	27	328.0	280.8	20.43	18.91	0.144	0.71
QST-30	30	328.1	280.6	20.44	18.90	0.145	0.79
QST-38	38	327.9	278.5	20.43	18.83	0.151	1.01
QST-61	61	328.1	279.9	20.44	18.88	0.147	1.62

In addition to the triaxial stress state caused by the deviation of the stress trajectories, bending stresses occur in the vicinity of unilateral corrosion pits due to a shift of the centroidal axis at the pit. This effect was observed in some experimental campaigns on bare reinforcing bars [2,6], indicating a significant influence on the stress–strain behaviour, and on concrete structures instrumented with fibre optic strain sensing [12], where the strains caused by the bending stresses were measured. Presumably, the superposition of bending stresses leads to a premature steel rupture in the case of unilateral corrosion when compared to an axisymmetrically corroded bar with equal cross-section loss: due to the non-uniform tensile stresses caused by bending, the ultimate elongation on the tensile side of the cross-section is reached while the average stress in the residual cross-section is below the tensile strength. However, a quantification is complicated by the triaxial stress state occurring additionally in the vicinity of the corrosion pit due to the short damage length. Hence, a parametric study based on FE-analyses would be required to account for both effects (similar to those carried out in this study for axisymmetric damage, but requiring much more computational resources).

1.3. Focus of this study

This study investigates the influence of a triaxial stress state on the apparent uniaxial stress–strain behaviour and material characteristics of reinforcing bars with local corrosion damage. It focuses on bare reinforcing bars exhibiting corrosion pits with a reasonably axisymmetric damage geometry, similar to that shown in Fig. 1 (a) for a naturally corroded bar. Unilateral (non-axisymmetric) pit geometries are deliberately excluded in this first step to clearly separate between the effects of a triaxial tensile stress state and the superimposed effects of bending stresses (see previous section). A future study addressing the combined effects of triaxiality and bending, as well as differences in pit morphologies between bare and embedded bars is envisaged by the authors.

An experimental campaign on reinforcing bars of two different steel types was conducted, with each specimen having an artificially created local damage of different lengths. The specimens were instrumented using a three-dimensional digital image correlation system, enabling the observation of the stress–strain behaviour in different regions near the pit, which are discussed and compared to simple engineering approaches for strain localisation. In a second step, the experiments were modelled with the FE software Ansys, using von Mises' J2-plasticity model beyond the yield point. The effects of the occurring triaxial stress state are discussed in detail. A comprehensive parametric study including 270 different datasets for each steel type demonstrates the influence of a triaxial stress state for varying geometrical parameters. Finally, a simplified modelling approach is presented, which allows estimating the stress–strain behaviour of an axisymmetrically corroded reinforcing bar accounting for the effects of the triaxial stress state.

1.4. Further effects

A considerable amount of reinforcing bars used since the 1990s [26] are produced as quenched and self-tempered (QST) bars, sold under the labels "Tempcore®" or "Thermex®". In the last step of their production process, these hot-rolled bars are quenched with water and then cooled under ambient conditions. During the cooling period, the hot core of the reinforcing bar tempers the quenched outer annulus. This process forms a reinforcing bar with distinct microstructure over the cross-section: The ferritic/perlitic core with high ductility but moderate strength is surrounded by a bainitic transition zone and a martensitic outer annulus with high strength but moderate ductility. The composed bar exhibits favourable material characteristics of higher strength and ductility [27–30]. However, QST reinforcing bars change their apparent material characteristics during the corrosion degradation process due to changes in the relative areas of the different microstructures.

This effect is well-investigated [25,31–35], and a simple model to consider this influence for corroded reinforcing bars is presented in [31], including different levels of approximation depending on the available material data. Within the present study, the mentioned model is used to describe the stress–strain behaviour of one of the investigated reinforcing steels. However, since an in-depth analysis of the effect of distinct microstructure is beyond the scope of this study, the reader is referred to [31] for a detailed model description and further information on this topic.

2. Experimental programme

The experimental campaign was designed to investigate the influence of a triaxial stress state in the vicinity of an axisymmetric cross-section reduction induced by corrosion. The diameter of the reinforcing bar samples was reduced axisymmetrically to isolate the effect of triaxial stresses on their load-deformation behaviour, see Sections 1.2 and 1.3. Such a damage geometry was found for some of the corroded reinforcing bars extracted from an existing Swiss cantilever retaining wall built in 1972 [12,36], see Fig. 1 (a).

The experimental campaign was carried out in the structural laboratory at ETH Zurich and comprised two test series with 7 specimens each. One series used reinforcing bars which were hot-rolled and later cold-worked (CW, Fig. 1 (b)), the other series used quenched and self-tempered reinforcing bars (QST, Fig. 1 (c)). The 500 mm long specimens originated from the same production batch per series, and batches were identical to those of [31,37]. The initial (nominal) diameter of the bars was reduced from $\varnothing = 20$ mm to a remaining (target) diameter of $\varnothing_c = 19$ mm over a distinct length L_c per specimen. The targeted cross-section reduction of 10% was chosen to ensure that the bar outside the damage zone still undergoes plastic deformation to attenuate the strain

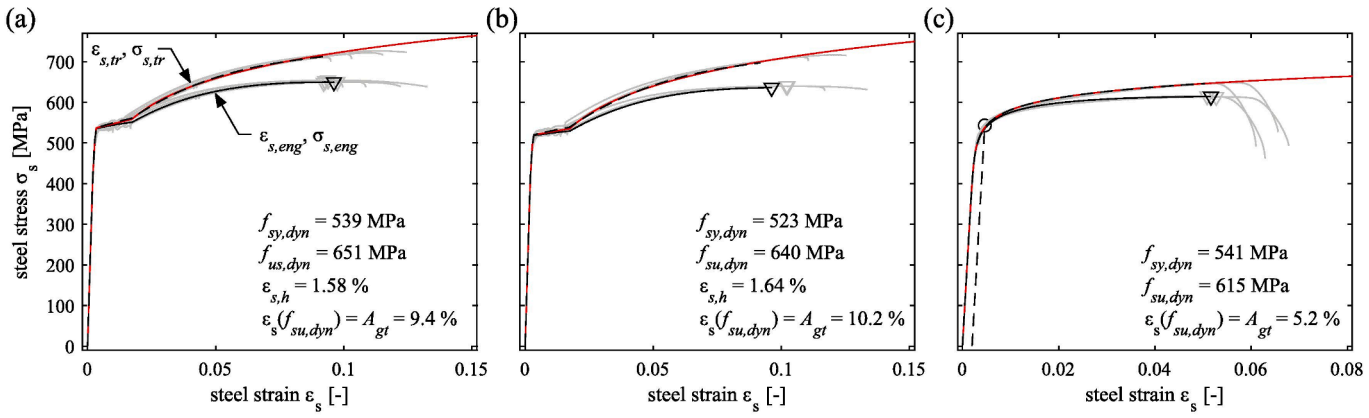

Fig. 2. Stress–strain relationships and material characteristics from standard tensile tests of (a) QST reinforcing bar ∅20, (b) QST reinforcing bar ∅19, (c) CW reinforcing bar ∅20. The plots show true and engineering stress–strain curves of the test samples (grey curves, $\varepsilon_{s,tr}$, $\sigma_{s,tr}$ and $\varepsilon_{s,eng}$, $\sigma_{s,eng}$, respectively), the steel characteristics (dynamic yield stress $f_{sy,dyn}$, dynamic tensile strength $f_{su,dyn}$ and corresponding strain A_{gt} (marked with a triangle), and strain at onset of hardening $\varepsilon_{s,h}$) and the corresponding constitutive relationships (black and red curves), see Section 3.2. (For interpretation of the references to colour in this figure legend, the reader is referred to the web version of this article.)

localisation. The diameter was reduced mechanically by machining on a lathe (turning). During turning, the specimens were constantly cooled to prevent heat inflow and an unintended alteration of steel microstructure and characteristics. The ratio $(L_c/2)/\varnothing_c$ varied between 0.4 and 1.6, which resulted in the damage lengths L_c reported in Table 1; note that the numbers of the specimen designation correspond to the damage length in millimetres. The geometry of all reinforcing bars was scanned before testing using a three-dimensional optical scanner (ATOS Core by GOM). The accurate measurements of initial and residual diameter allowed to precisely determine the cross-sectional areas of the bars (see Table 1). With the effective initial diameter being a bit larger than 20 mm and the precision of the mechanical diameter reduction, the effective cross-section loss was slightly higher than targeted.

The specimens were tested deformation controlled until failure in a universal testing machine at a constant strain rate of 10^{-4} s^{-1} (Fig. 1 (d)). Load introduction heads with spherical hinges were installed on the testing machine to minimise unintentional bending moments in the specimens due to geometrical misalignment of either the machine heads or the clamping, which can hardly be avoided and could otherwise have affected the test results. Threads were provided at the specimen ends, which were connected to the load introduction heads using spherical washers and nuts. A three-dimensional digital image correlation system (DIC) with two ProSilica GT600-cameras containing a sensor of 6576 × 4384 Px = 29MPx was used to capture the specimen deformations. To this end, the specimens were sandblasted and subsequently painted white and speckled black (see Fig. 1 (b) to (d)). The cameras were placed vertically at a distance of 900 mm from the specimen, with an inter-camera distance of 300 mm to enable optimal correlation of the curved bar surface. The system setup resulted in a resolution of approximately 0.014 mm/px. The data was post-processed with a subset size of 29 px and a step size of 7 px, providing data points at a distance of 0.4 mm.

Standard tensile tests were conducted on 1200 mm long bar samples at a constant strain rate of 10^{-4} s^{-1} to determine the material characteristics of the reinforcing bars, using an LVDT of 300 mm gauge length to measure the deformations. Fig. 2 shows the steel stress–strain relationships (true and engineering strains and stresses, $\varepsilon_{s,tr}$, $\sigma_{s,tr}$ and $\varepsilon_{s,eng}$, $\sigma_{s,eng}$, respectively) together with the corresponding characteristics and the constitutive models (see Section 3.2) for (a) the QST reinforcing bars with an initial diameter of 20 mm, (b) the QST reinforcing bars with a reduced diameter of 19 mm, and (c) the CW reinforcing bars (diameter 20 mm).

Due to the different production processes, the CW reinforcing steel has a perlitic/ferritic microstructure over its entire cross-section, whereas the QST reinforcing steel of this specific sample consists of a martensitic outer annulus (for $r \geqslant 0.85R$), a bainitic transition zone ($0.85R > r \geqslant 0.65R$) and a perlitic/ferritic core ($r < 0.85R$) [31], with r = distance from bar centre and $R = \varnothing/2$ = outermost radius. The mechanical characteristics of the different microstructural layers determined in [31] are summarised in Table 2. Evidently, due to the large difference in the mechanical characteristics of the distinct layers, the QST bar changes its overall mechanical characteristics with increasing cross-section loss. To capture this effect, separate constitutive relationships were used in the analysis of the experimental results of the QST specimens ∅20 and ∅19 (determined experimentally for this batch in [31]), as shown in Fig. 2 (a) and (b); the model proposed in [31] linking the cross-section loss to the remaining mechanical characteristics of the composed bar was used for the parametric analysis, with the layer characteristics reported in Table 2 serving as input.

Although originating from the same production batch as the specimens in [31,37], the plotted stress–strain relationships and the steel characteristics were determined from additional tensile tests conducted near-term to the experiments to avoid any influence of strain ageing, which commonly affects CW reinforcement. This effect is indeed evident

Table 2
Material characteristics of perlitic/ferritic core, martensitic outer annulus, and original (composed) reinforcing bar as experimentally determined in [31] for the QST series of the present study (same production batch).

		engineering values			true values		
		core	outer annulus	composed bar ∅20	core	outer annulus	composed bar ∅20
yield strain	[10^{-3}]	2.0	5.5	4.7	2.0	5.5	4.7
strain at hardening onset	[10^{-3}]	17.5	–	15.8	17.0	–	15.7
strain at peak stress	[10^{-3}]	128.5	96.2	95.0	121.0	92.0	91.0
yield stress	[MPa]	409	703	539	410	707	542
stress at hardening onset	[MPa]	409	–	551	416	–	563
peak stress	[MPa]	555	777	651	627	852	712

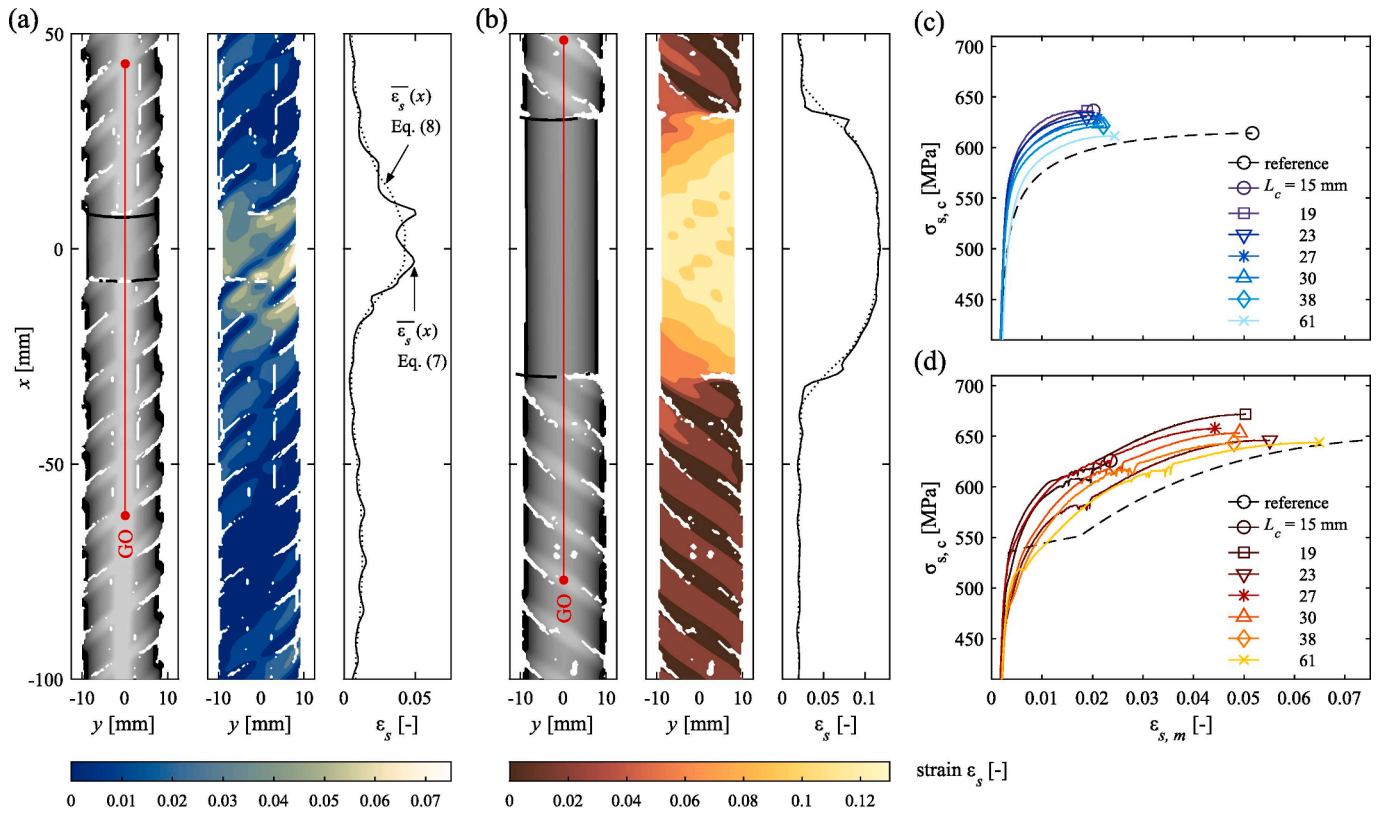

Fig. 3. Strain measurements using DIC of Specimens (a) CW-15 and (b) QST-61, showing the bar geometry (grey), the full-field strains at peak load (coloured), and the corresponding mean strain over the bar width according to Equation (7); stress-mean strain curves $\sigma_{s,c}$ vs $\varepsilon_{s,m}$ of all specimens of (c) CW and (d) QST reinforcing bars using the virtual gauges GO indicated in red in (a) and (b), with a length L_{tot} reported in Table 3. Note: white areas in (a) and (b) could not be correlated. (For interpretation of the references to colour in this figure legend, the reader is referred to the web version of this article.)

when comparing the characteristics presented in Fig. 2 (c) to those reported in [37] (e.g., increase of yield stress by 5% over time). No strain ageing effect was observed for the QST reinforcing bars ∅20 (comparing the results of Fig. 2 (a) to those reported in [31,37]) which allowed to adopt the relationship and characteristics of the QST bar ∅19 (Fig. 2 (b)) directly from [31].

3. Definitions and basic theoretical models

3.1. Used definition of stress

Throughout this paper, the apparent uniaxial stress in the corroded damage zone (subscript *c*; in general and at peak load) is defined as

$$\sigma_{s,c} = \frac{F}{A_{s,c}} \qquad \sigma_{s,c,max} = \frac{F_u}{A_{s,c}} \tag{1}$$

and the stress in the undamaged part of the bar (uncorroded regular cross-section, subscript *uc*) as

$$\sigma_{s,uc} = \frac{F}{A_s} \qquad \sigma_{s,uc,max} = \frac{F_u}{A_s} \tag{2}$$

with F, F_u = load and peak load, and A_s, $A_{s,c}$ = initial and reduced cross-sectional areas of the bar (Table 1). The relative cross-section loss is defined as

$$\zeta = \frac{A_s - A_{s,c}}{A_s} \in [0,1] \tag{3}$$

and hence, the stress in the damaged and undamaged parts is related by equilibrium

$$\sigma_{s,uc} = \sigma_{s,c}(1-\zeta) \tag{4}$$

The corresponding strains in the damaged and undamaged part, $\varepsilon_{s,c}$ and $\varepsilon_{s,uc}$, follow from the stress–strain relationships of Fig. 2 or any constitutive material relationship.

3.2. Constitutive material relationships

The stress–strain relationships of the QST reinforcing bars ∅20 and ∅19 are approximated using the constitutive model described in [31]. The input parameters for the model evaluation (i.e., characteristics of the distinct microstructure layers perlite/ferrite, bainite, and martensite, as well as their amount on the total cross-sectional area) are also taken from [31], since the specimens of both studies originate from the identical production batch, and no strain ageing was observed in the QST bars. The model response is shown in Fig. 2 (a) and (b) as solid black lines, virtually identical to the material test results.

The following constitutive relationship is used to approximate the results of the material tests of the CW reinforcing bars:

$$\varepsilon_s(\sigma_s) = \frac{\sigma_s}{E_s} + \left(\frac{c_1}{c_2 - \sigma_s}\right)^{1/c_3} + c_4$$
$$c_1 = \frac{K c_4^{c_3} f_{su}}{K - c_4^{c_3}}$$
$$c_2 = \frac{c_1}{c_4^{c_3}} \quad (5)$$
$$K = \left(A_{gt} - \frac{f_{su}}{E_s} + c_4\right)^{c_3}$$
$$\varepsilon_s,\ A_{gt} \text{ in } [\ -\ ],\ \sigma_s,\ f_{su},\ E_s \text{ in [MPa]}$$

with f_{su}, A_{gt} = tensile strength and corresponding strain from the material tests, E_s = 205 GPa = steel Young's modulus, and c_3, c_4 = model parameters. The proposed relationship extends the one proposed by Ramberg and Osgood [38] such that the curve accurately captures the behaviour of modern European reinforcing steel. The model parameters were determined such that the material tests are closely approximated, which resulted in $c_3 = 3.2{\cdot}10^{-10}$ and $c_4 = 2.0{\cdot}10^{-14}$ (in true stresses and true strains, which can be reformulated to engineering stresses and strains, see Section 5.1). The model response is shown in Fig. 2 (c) as solid black line.

3.3. Strain localisation model (SLM)

Strain localisation is modelled by idealising the bars as tension members consisting of several sub-members with different lengths, cross-sectional areas and stress–strain behaviour, which are serially connected and, hence, subjected to an equal normal force. The stresses in the sub-members at any given load are determined with respect to their actual cross-sectional areas (e.g., using Equations (1) and (2)). The corresponding strains follow from the constitutive material model (e.g., Equation (5)), and the sub-member elongations are obtained by multiplying the strains with the sub-member length. Summing up the elongations of all sub-members and dividing by the total length yields the mean strain of the entire tension member. For a reinforcing bar of total length L_{tot} and initial cross-sectional area A_s, which contains a locally reduced cross-sectional area $A_{s,c}$ over the damage length L_c, the mean strain obtained by the SLM is (using the notation of Equations (1)-(3)):

$$\varepsilon_{s,m}^{SLM}(\sigma_{s,c}) = \frac{L_c \varepsilon_s(\sigma_{s,c}) + (L_{tot} - L_c)\varepsilon_s(\sigma_{s,uc})}{L_{tot}} = \frac{L_c \varepsilon_s(\sigma_{s,c}) + (L_{tot} - L_c)\varepsilon_s(\sigma_{s,c}(1-\zeta))}{L_{tot}} \quad (6)$$

where $\varepsilon_s(\sigma_s)$ denotes the constitutive material model. A detailed description of the concept, including example calculations and accounting for tension stiffening in concrete tension members, can be found in [13]. An identical model was successfully applied to bare reinforcing bars with artificially reduced cross-sections by Zeng et al. [11].

4. Experimental results

4.1. Strain measurements and influence of ribs

The field of view of the DIC setup described in Section 2 covered almost the entire projection of half the circumferential bar surface, as illustrated in Fig. 3 (a) and (b) for the surface geometry of the Specimens CW-15 and QST-61 (in grey). The correlation of the images of the two cameras was very satisfying; only the white areas below or above a rib could not be correlated since they were hidden by the corresponding rib and out of sight for either of the cameras.

DIC provides deformation measurements of a specimen surface, which can deviate from the average specimen deformation over the cross-section, especially if the surface exhibits elevations such as the ribs of a reinforcing bar. This issue can be observed in the full-field strains at peak load shown in colour in Fig. 3 (a) and (b). In the undamaged part, the location of the areas exhibiting small strains matches the location of the ribs perfectly, indicating that the ribs deform much less than the bar on average. The measured strains on the ribs do not necessarily need to represent the specimen deformation over the cross-section, which is evident when comparing to the strains on the left and right side of a rib (at a horizontal cross-section, e.g., at $x = -50$ mm). Similar effects are known from other near-surface measurement techniques, e.g., from fibre optic strain sensing on reinforcing bars, see [39,40].

Table 3
Lengths L_{tot} of Gauge GO (Fig. 3) per specimen, bridging the damaged section with length L_c and instrumenting a length L_{uc} with regular cross-section.

Specimen	L_c [mm]	L_{uc} [mm]	L_{tot} [mm]
CW-15	15	90	105
CW-19	19	86	105
CW-23	23	73	96
CW-27	27	73	100
CW-30	30	73	103
CW-38	38	79	117
CW-61	61	68	129
QST-15	15	88	103
QST-19	19	82	101
QST-23	23	93	116
QST-27	27	87	114
QST-30	30	81	111
QST-38	38	89	127
QST-61	61	65	126

To overcome this issue, the mean strain over the instrumented bar width is calculated as

$$\overline{\varepsilon_s}(x) = \frac{\int_{y_{min}}^{y_{max}} \varepsilon_s(x,y)dy}{(y_{max} - y_{min})} \quad (7)$$

Results obtained from Equation (7) are shown as solid lines in Fig. 3 (a) and (b) for the strains at peak load. While the mean strain is a simple and intuitive measure to qualitatively compare the strains of different bar sections or between different specimens at equal load, it is inadequate to determine strains and stresses quantitatively since the ribs still affect the calculated strain distribution $\overline{\varepsilon_s}(x)$ (as seen in Fig. 3 (a) and (b)), as a specific strain value $\overline{\varepsilon_s}(x)$ depends on the number of measurement points laying on or next to a rib.

A more robust measure for strains was found to be the integral of axial strains along the bar axis (or a parallel to the latter) over an axial distance equal to the rib spacing, divided by this distance (essentially corresponding to virtual strain gauges with the rib spacing as base length). For any lateral position $y = y_1$, this strain measure is defined as

$$\overline{\varepsilon_s}(x, y = y_1) = \frac{\int_{x-c/2}^{x+c/2} \varepsilon_s(x, y = y_1)dx}{c} \quad (8)$$

with c = rib spacing. The ribs only negligibly influence the results since the number of measurement points laying on or next to a rib is approximately constant for all locations x. However, if Equation (8) is used continuously over x, it strongly underestimates steep strain gradients, e.g., in the cross-section transition at the end of the damage zone (see Fig. 3). To avoid this issue, discrete virtual gauges with gauge length = rib spacing were placed along the bar, paying attention that no gauge overlaps the cross-section transition (except for the gauge GO in Fig. 3, which spans the entire bar), and strains are calculated in this paper according to Equation (8) for the virtual gauges.

The lengths L_{tot} of the longest gauge GO (shown in red in Fig. 3 (a) and (b)), bridging the damaged section with length L_c and a length L_{uc} with regular cross-section, was approximately constant for all experiments; the exact values are reported in Table 3. L_{tot} was chosen such that the gauge endpoints were located at least one diameter away from the

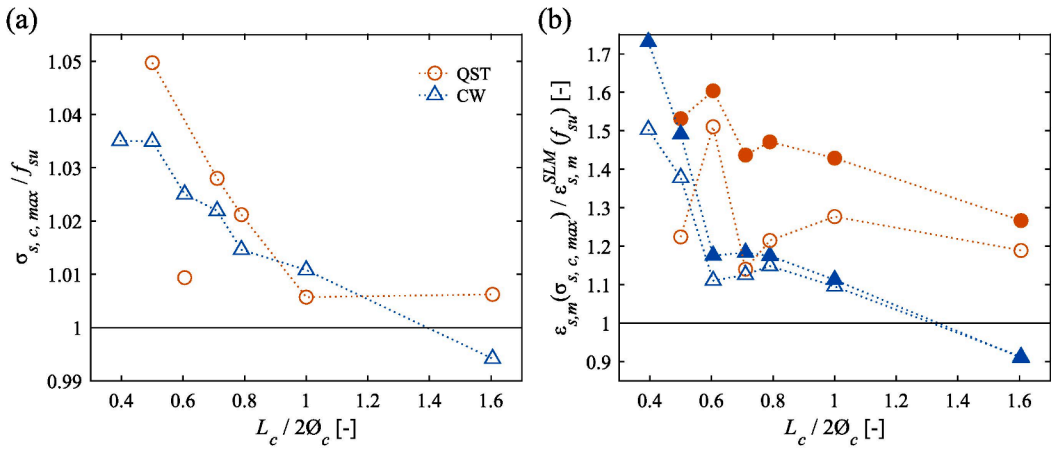

Fig. 4. Experimental results of tension tests: (a) Peak stress normalised with uniaxial tensile strength and (b) mean strain at peak stress, normalised with mean strain predicted by SLM (Equation (6)). Filled markers result from evaluating Equation (6) with $\sigma_{s,uc} = (1-\zeta)f_{su}$, and empty markers for $\sigma_{s,uc} = (1-\zeta)\sigma_{s,c,max}$.

damage zone (where possible two or more diameters, but observing the limitation by the field of view of the cameras).

Fig. 3 (c) and (d) show the stress-mean strain curves (σ_s vs $\varepsilon_{s,m}$) of all CW- and QST-specimens, respectively, with $\varepsilon_{s,m}$ = strain measured at the virtual gauge GO. The strain at peak stress is reduced by approximately 50% compared to the corresponding $A_{gt} = 5.2\%$ (CW), 9.4% (QST, ∅19) and 10.2% (QST, ∅20, see Fig. 2) of the undamaged bars (dashed lines in Fig. 3(c) and (d)), which is a direct consequence of strain localisation. However, the variation of the strain at peak stress among the same steel type is remarkably small, considering their different damage lengths L_c (except for QST-15, which failed prematurely). Moreover, the apparent uniaxial peak stress appears to increase with decreasing damage length L_c, which is remarkable since the cross-section reduction was equal for all specimens (small variations in the cross-sectional area, see Table 1, were accounted for in determining the stresses). These effects are attributed to a triaxial stress state in the vicinity of the damage zone, which is further analysed in the following sections.

4.2. Increase in tensile strength and corresponding deformation

Fig. 4 (a) shows the peak stress in the damage zone measured in the experiments, normalised with the tensile strength f_{su} of the material tests, vs the normalised damage length. The actual cross-sectional areas (Table 1) were used to determine the stresses, and the tensile strength of the reduced cross-section ∅19 (listed in Fig. 2 (b)) for the normalisation of the results of the QST reinforcing bars. While the ratio $\sigma_{s,c,max}/f_{su}$ is close to 1 (±1%) for $L_c/(2\varnothing_c) \geqslant 1$, a significant increase in the peak stress is observed for both steel types with decreasing damage length, with peak stresses exceeding the material tensile strength by up to 5%.

In Fig. 4 (b), filled blue and red markers indicate the observed strains at peak stress $\varepsilon_{s,m}(\sigma_{s,c,max})$ of the virtual gauge GO (Fig. 3 and Table 3), plotted vs the normalised damage length. The measured strains are normalised with the strains expected according to the SLM (Equation (6)), assuming $\sigma_{s,c} = f_{su}$. For the QST reinforcement (filled red markers), a steady increase of the strain at peak stress, compared to the theoretical strains of the SLM, is observed with decreasing damage length, with a pronounced strain increase even for the longest damage length ($L_c/(2\varnothing_c) = 1.6$). For the CW-reinforcement (filled blue markers), the increase in peak strain is less pronounced for $L_c/(2\varnothing_c) \geqslant 0.6$ but increases sharply for shorter damage lengths.

Evidently, the strains at peak stress in the undamaged parts were higher than assumed by the calculations underlying the solid markers (using $\sigma_{s,c} = f_{su}$) due to the increased peak stress for shorter damage lengths (see Fig. 4 (a)). To eliminate this effect and visualise a potentially altered stress–strain behaviour, the actually measured load is considered in a second step for determining the theoretically expected

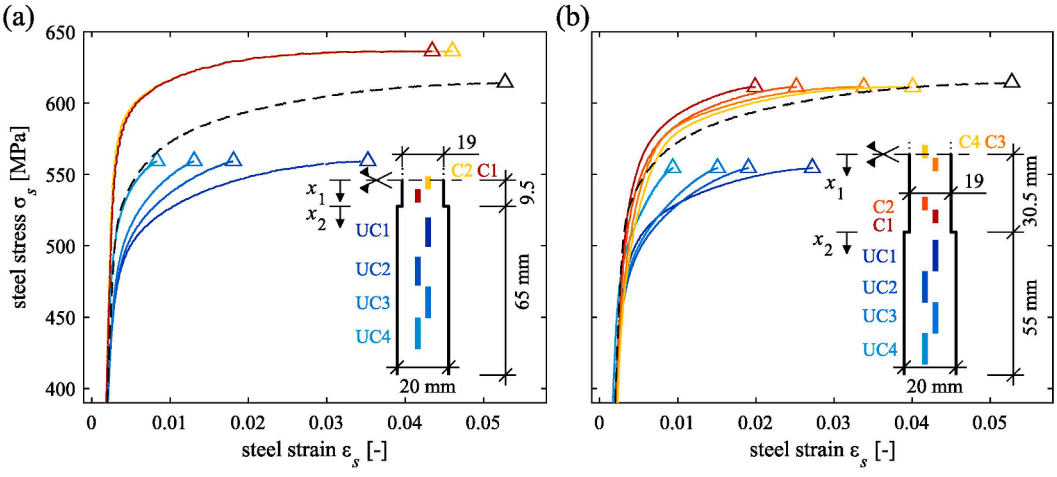

Fig. 5. Stress–strain curves of different virtual gauges along the bar axis in the damage zone (red, yellow) and the adjacent undamaged zone (blue) for the Specimens (a) CW-19 and (b) CW-61, with schematic positions of the gauges shown to the right. The dashed black lines represent the reference curve of the material tests. Stresses refer to the reduced cross-sectional area in the damage zone and to the initial cross-sectional area in the undamaged part according to Equations (1) and (2), and Table 1. (For interpretation of the references to colour in this figure legend, the reader is referred to the web version of this article.)

Table 4
Gauge length *GL* and position of gauge centre of the gauges shown in Figs. 5 and 6 (x_1=distance from damage zone centre, x_2 = distance from cross-section transition, see Figs. 5 and 6).

Gauge	CW-15			CW-61			QST-15			QST-61		
	GL[mm]	x_1[mm]	x_2[mm]	*GL*[mm]	x_1[mm]	x_2[mm]	*GL*[mm]	x_1[mm]	x_2[mm]	*GL*[mm]	x_1[mm]	x_2[mm]
C4				5.3	0.2	−30.3				5.2	0.2	−30.2
C3				5.0	5.3	−25.2				4.8	5.2	−25.3
C2	3.8	0.3	−9.2	5.0	20.1	−10.4	4.9	0.0	−9.5	5.2	20.2	−10.3
C1	4.2	4.3	−5.2	5.6	25.4	−5.1	4.2	4.6	−4.9	5.6	25.6	−4.9
UC1	10.9	17.6	8.1	10.9	38.8	8.3	13.6	20.9	11.4	10.8	37.3	6.8
UC2	10.9	32.7	23.2	12.0	50.2	19.7	12.4	33.9	24.4	12.9	45.8	15.3
UC3	12.0	44.1	34.6	11.9	62.1	31.6	12.7	46.4	36.9	12.4	58.4	27.9
UC4	11.9	56.1	46.6	12.2	74.2	43.7	12.3	58.9	48.5	12.7	71.0	40.5

strains, replacing the term $\sigma_{s,uc} = f_{su}(1-\zeta)$ in Equation (6) with $\sigma_{s,uc} = \sigma_{s,c,max}(1-\zeta)$. The results are depicted in Fig. 4 (b) with empty markers in red and blue for the QST and CW reinforcement, respectively. While the strain increase compared to the predictions of the SLM are somewhat reduced, particularly at short damage lengths, the overall tendencies remain the same, indicating an altered stress–strain behaviour.

4.3. Analysis of stress–strain behaviour inside and close to the damage zone

Fig. 5 shows the stress–strain curves of several virtual strain gauges for the specimens (a) CW-19 (short damage length) and (b) CW-61 (long damage length). The gauges in the undamaged part span one rib distance (as suggested in Section 4.1), while the gauge lengths in the damage zone without ribs are shorter (11–12 mm and 5 mm, respectively); the gauge positions and lengths are shown schematically in the figures and are reported in Table 4. Stresses (referred to the reduced cross-sectional area, Equation (1)) and strains in the damage zone are depicted in red and yellow; stresses (referred to the initial cross-sectional area, Equation (2)) and strains in the adjacent undamaged parts are shown in blue. The stress–strain curve of the corresponding material test is shown as a dashed black curve for comparison, and the peak load is marked with triangles.

In Specimen CW-19 (short damage length, Fig. 5 (a)), the curves of the gauges in the damage zone (yellow and red) almost coincide, with slightly smaller strains at peak stress of the gauge closer to cross-section

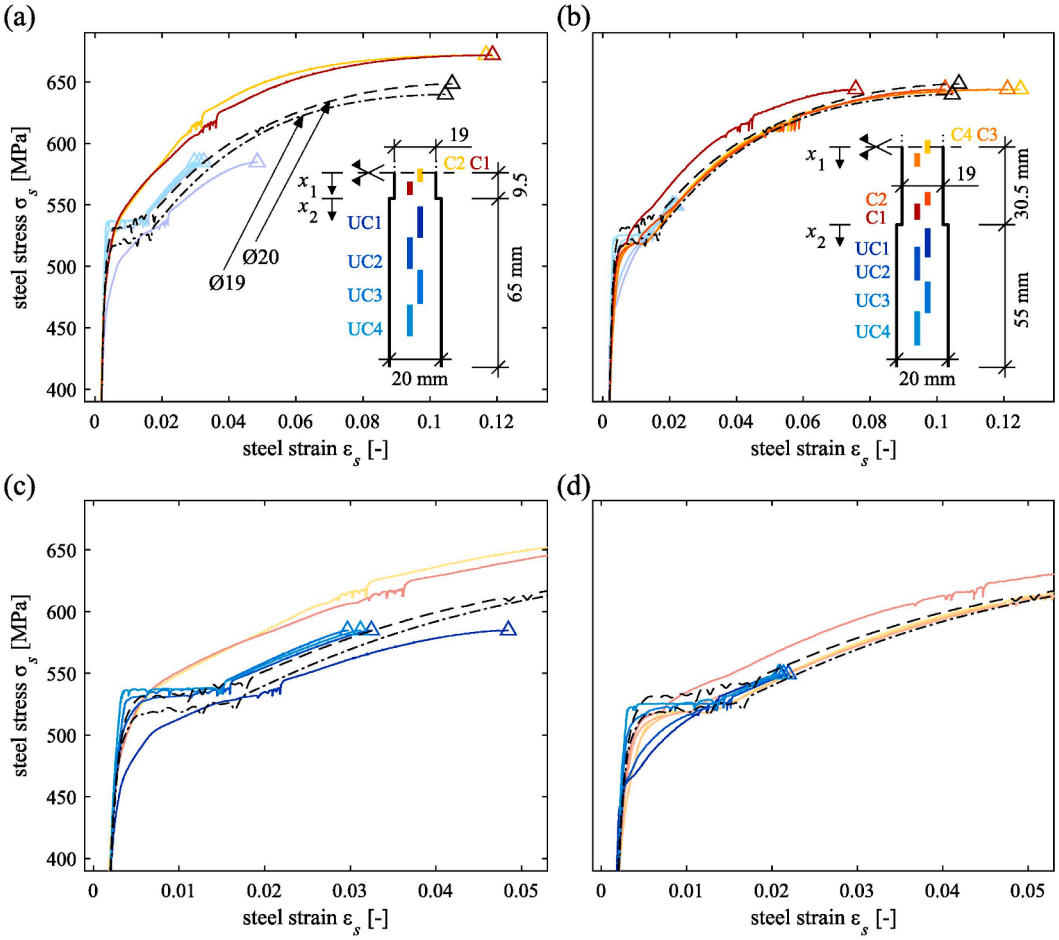

Fig. 6. Stress–strain curves of different virtual gauges along the bar axis in the damage zone (red, yellow) and the adjacent undamaged zone (blue) for the Specimens (a) QST-19 and (b) QST-61, with schematic positions of the gauges shown to the right. The dashed black lines represent the reference curve of the material tests for ⌀20, and the dash-dotted lines that for ⌀19. Stresses refer to the reduced cross-sectional area in the damage zone and to the initial cross-sectional area in the undamaged part according to Equations (1) and (2), and Table 1. (For interpretation of the references to colour in this figure legend, the reader is referred to the web version of this article.)

transition (C1, red). The stresses of both curves are significantly higher than in the material tests, and the apparent uniaxial yield stress and tensile strength are clearly increased. After passing the yield point, the curves flatten pronouncedly and continue almost horizontally until the peak stress. On the other hand, the stress–strain curves in the undamaged part exhibit a significantly softer behaviour compared to the material test, with lower stiffnesses and, accordingly, higher strains at peak stress the closer the gauges are located to the damage zone. Hence, while the curve of Gauge UC4 (light blue), away from the damage zone, closely follows the material reference curve, the strains of UC1 are roughly four times higher at equal stress. The strain of UC1 at peak stress is thus similar to the one of Gauge C1 in the damage zone although the cross-sectional area at UC1 was roughly 17% higher than at C1 in the damage zone (see Table 1).

In Specimen CW-61 (long damage length, Fig. 5 (b)), other than in Specimen CW-19, the peak stresses in the damage zone are almost identical to the tensile strength of the material tests. Still, the stress–-strain curves in the damage zone show a stiffer behaviour closer to the cross-section transition (Gauges C4 to C1, yellow to red): while Gauge C4 in the middle of the damage zone exhibits a stress–strain behaviour similar to the reference curve, the strain at peak stress of Gauge C1 is reduced approximately by a factor of 2. The curves of the gauges in the undamaged part (UC1 to UC4, blue) are very similar to the corresponding curves of Specimen CW-19 (Fig. 5 (a)), with a softer stress–-strain behaviour close to the damage zone. Again, the strains in Gauge UC4 (light blue) are similar to the reference curve, whereas the strains in Gauge UC1 (dark blue) are comparable to those in the damage zone, and even higher than the strains of Gauges C1 and C2. The strains at peak stress measured in the Gauges UC2 to UC4 are almost identical for both specimens CW-19 and CW-61, irrespective of the different damage lengths.

Fig. 6 (a) and (b) show the results of Specimens QST-19 and QST-61, respectively, with a zoom to the yield point in (c) and (d). As a reference, the dashed lines show the stress–strain curve of the material test on a bar ∅20, applying to the results of the gauges in the undamaged part (UC1 to UC4), and the dash-dotted lines refer to the material test on a bar with reduced diameter ∅19, applying to the results of the gauges in the damage zone (C1 to C4).

The results obtained for Specimen QST-19 (short damage length, Fig. 6 (a)) are similar to those of Specimen CW-19 in Fig. 5 (a). The strains in Gauge C1 are similar to those of Gauge C2, and both curves show a stiffer behaviour at the beginning of the inelastic phase. Nevertheless, strains at peak stress are even higher in this specimen than in the reference test, and the peak stresses are again increased compared to the tensile strength of the reference test. The stress–strain curves of the Gauges UC1 to UC4 in Fig. 6 (c) in the adjacent undamaged part differ less from the reference curve than those in Fig. 5 (a), except for Gauge UC1 closest to the damage zone, which clearly exhibits a softer behaviour.

The stress–strain curves of the gauges in the damage zone (red, yellow) of Specimen QST-61 (long damage length, Fig. 6 (b)) follow the curves of the reference test even closer than in Specimen QST-19. Nevertheless, a stiffer behaviour is observed closer to the cross-section transition (C4 to C1), with the Curve C1 (red) differing significantly, exhibiting merely about 60% of the strain at peak stress compared to C4. The curves of the gauges in the adjacent undamaged part UC1 to UC4 differ much less than in Specimen CW-61 (Fig. 5 (b)) and closely follow the reference curve in the elastic range and at hardening onset.

An interesting observation in Fig. 6 is the loss of the yield plateau (i.e., of the approximately horizontal part of the black reference stress–-strain curve between the yield point and the hardening onset). The same observation was made in tension tests of reinforcing bars with natural, unilateral corrosion pits [23]. In the undamaged part, the yield plateau is absent for all gauges close to the cross-section transition (UC1, UC2, C1 and C2). For UC1 of QST-19 and UC1 and UC2 of QST-61, the yield point is lowered from 540 MPa to approximately 450 to 470 MPa, directly followed by the strain hardening phase. Except for UC1 of QST-19, the curves pass the point $\left(\varepsilon_{sh},\ f_{sy}\right)$ and then follow the reference curves again. This stress–strain behaviour contrasts the one of gauges further away from the damage zone (UC3, UC4), which closely follow the reference curve and exhibit a yield plateau. Similarly, in all gauges of the damage zone close to the cross-section transition (C1 and C2 for QST-19 and C1 for QST-61), the strain hardening phase directly seems to follow the yield point, while the curves observed at Gauges C3 and C4 in QST-61, away from the transition, again follow the reference curve and exhibit a yield plateau.

A macroscopically visible yield plateau is related to the occurrence of Lüders bands and is associated with discontinuous yielding. Presumably, the triaxial stress state at the cross-section transition influences the deformation behaviour of crystal grains in the steel, preventing macroscopically visible discontinuous yielding. The phenomenon is further investigated in Section 5.5, after analysing the triaxial stress state near a local damage.

5. Analysis of triaxial stress state near local damages

5.1. Introduction and FE model description

For the assessment of the experiments, the reinforcing bars were modelled with the FE-software Ansys Mechanical as concatenated smooth cylinders, with two cylinders of diameter ∅ enclosing a cylinder of length L_c and reduced diameter $\varnothing_c$ (diameters according to Table 1). The composed bar has a total length of 200 mm and is fixed at one end, whereas an increasing displacement is imposed at the other end. The structure is meshed with PLANE183-elements at a size of 1.0 mm, which allows to exploit the axial symmetry and reduce the calculation time. Von Mises' J2-plasticity model (see Section 1.3) with isotropic hardening was implemented as a material model, and the analyses accounted for geometrical nonlinearity. A possible mesh-size dependency was not analysed since a similar study reported no such influence for the chosen mesh size [20].

For material input, the engineering stress–strain relationships shown in Fig. 2 need to be converted to true values. True strains result from considering the deformations on a differential element, leading to $d\varepsilon_{tr} = dl/l$. For true stresses, the force is referred to the actual cross-sectional area, which decreases with increasing axial deformation due to volume conservation. The conversion can be approximated by (see, e.g., [41])

$$\begin{aligned}\varepsilon_{s,tr} &= \ln\left(1+\varepsilon_{s,eng}\right)\\ \sigma_{s,tr} &= \sigma_{s,eng}\left(1+\varepsilon_{s,eng}\right)\end{aligned} \tag{9}$$

Assuming a homogeneous bar (no variation of mechanical properties along the bar axis), Equation (9) can be applied to the data of the material tests up to the onset of necking, which occurs after having reached the tensile strength. Fig. 2 shows the converted stress–strain curves of the material tests in grey and the constitutive material models in true values as dashed black lines.

Following the concept of [20], the input material curve is not limited to the tensile strength and the corresponding strain, but extrapolated from the constitutive relationships (formulated in true values) up to $\varepsilon_{s,tr} = 0.2$. Since the application range of the constitutive relationships is limited to the tensile strength and cannot be evaluated beyond this point, a logarithmic equation of the form

$$\begin{aligned}&\sigma_{s,tr} = b_1 \ln\left(\varepsilon_{s,tr}\right) + b_2\\ &\varepsilon_{s,tr} \text{ in } [\text{ - }],\ \sigma_{s,tr} \text{ in } [\text{MPa}]\end{aligned} \tag{10}$$

is fitted to the constitutive relationships in the hardening branch, i.e., in the range $\left[\varepsilon_{sh},\ A_{gt}\right]$ for the QST reinforcement and $\left[0.02,\ A_{gt}\right]$ for the CW reinforcement, with the parameters b_1 and b_2 summarised in Table 5. The resulting curves are shown in Fig. 2 as solid red lines. The second

Table 5
Fitting parameters for extrapolation of the hardening branch of constitutive material curves according to Equation (10).

Material constitutive relationship	b_1 [-]	b_2 [-]
CW	37.9	759.4
QST, ⌀20	94.7	942.6
QST, ⌀19	98.8	935.7
QST, ⌀19.5	96.7	939.2
QST, ⌀18.4	101.4	931.3
QST, ⌀17.9	104.1	926.6
QST, ⌀17.3	107.2	921.2
QST, ⌀16.7	108.9	910.5
QST, ⌀16.1	110.5	901.9
QST, ⌀15.5	112.1	894.1
QST, ⌀14.8	113.5	887.5
QST, ⌀14.1	114.9	882.5
QST, ⌀13.4	115.9	879.9
QST, ⩽⌀12.7	116.3	879.9

part of Table 5 contains the parameters for bars with a cross-section reduction beyond 19 mm, which are used for the parametric study in Section 6.

The force–elongation diagram resulting from the FE analyses is not monotonically increasing, as one might assume from the input material relationship. Since the FE-analysis considers the lateral contraction of the bar in the damage zone due to the high axial strains, the cross-section is continuously reduced with increasing axial deformation, and beyond a certain elongation, the force decreases despite that the axial stresses keep increasing. The elongation at the peak load – similar to the onset of necking in a tensile test – is considered representative for comparison with the experimental results.

5.2. Comparison of experiments with different models

Fig. 7 compares the force-mean strain curves obtained from the experiments (black) with the response of the SLM (blue, see Section 3.3) and the FE analyses of Section 5.1 for the CW (Fig. 7 (a) to (c)) and the QST reinforcement (Fig. 7 (d) to (f)) with damage lengths L_c = 15, 19, and 61 mm. The markers indicate the peak loads. The results of the remaining experiments with L_c = 23, 27, 30, and 38 mm are enclosed in the appendix. The gauge lengths L_{tot} used for evaluating the experimental data are reported in Table 3 and indicated in Fig. 7. Equation (6) is used for the SLM in combination with the constitutive material relationships of Section 3.2 and Table 1.

The results of Fig. 7 (a), (b), and (e) confirm the observation of Section 4.2 that the SLM strongly underestimates the strain at peak stress (up to 40%) for short damage lengths and, to a minor extent, also the peak stress. With increasing damage length, the accuracy of the SLM increases (see also Fig. A1), with the SLM being almost identical to the experimental results in Fig. 7 (c) for L_c = 61 mm. In contrast, the responses of the FE analyses capture the experimental curves for all damage lengths regarding curve shape, peak stress, and corresponding strain, except for Specimen QST-15 (Fig. 7 (d)), which failed prematurely. Accordingly, both models overestimate the peak stress and elongation of this experiment.

The results of the FE analyses support the hypothesis that the triaxial stress state at the cross-section transition considerably alters the stress–strain behaviour of reinforcing bars containing local corrosion damage. The hypothesis is further confirmed by the increasing prediction accuracy of the SLM for longer damage lengths, where the local effects of the transition zones become less relevant.

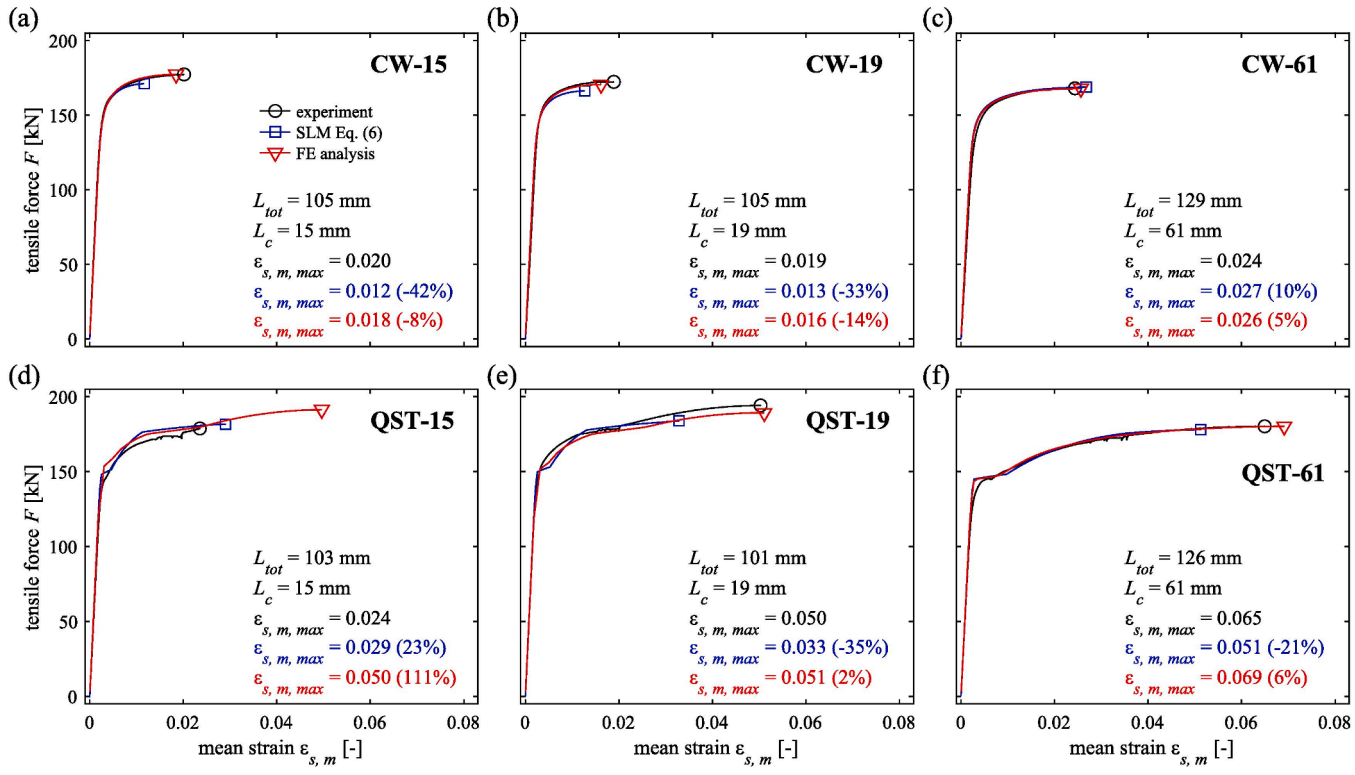

Fig. 7. Comparison of experimental results (black) with the SLM (Equation (6), blue) and the FE analyses (red): (a)-(c) Series CW; (d)-(f) Series QST, specimens with damage lengths L_c = 15, 19, and 61 mm. The markers indicate the peak loads. Additionally, the total gauge length L_{tot} and the mean strain at peak load $\varepsilon_{s,m,max}$ are reported, as well as the relative deviation between the models and the experimental result. (For interpretation of the references to colour in this figure legend, the reader is referred to the web version of this article.)

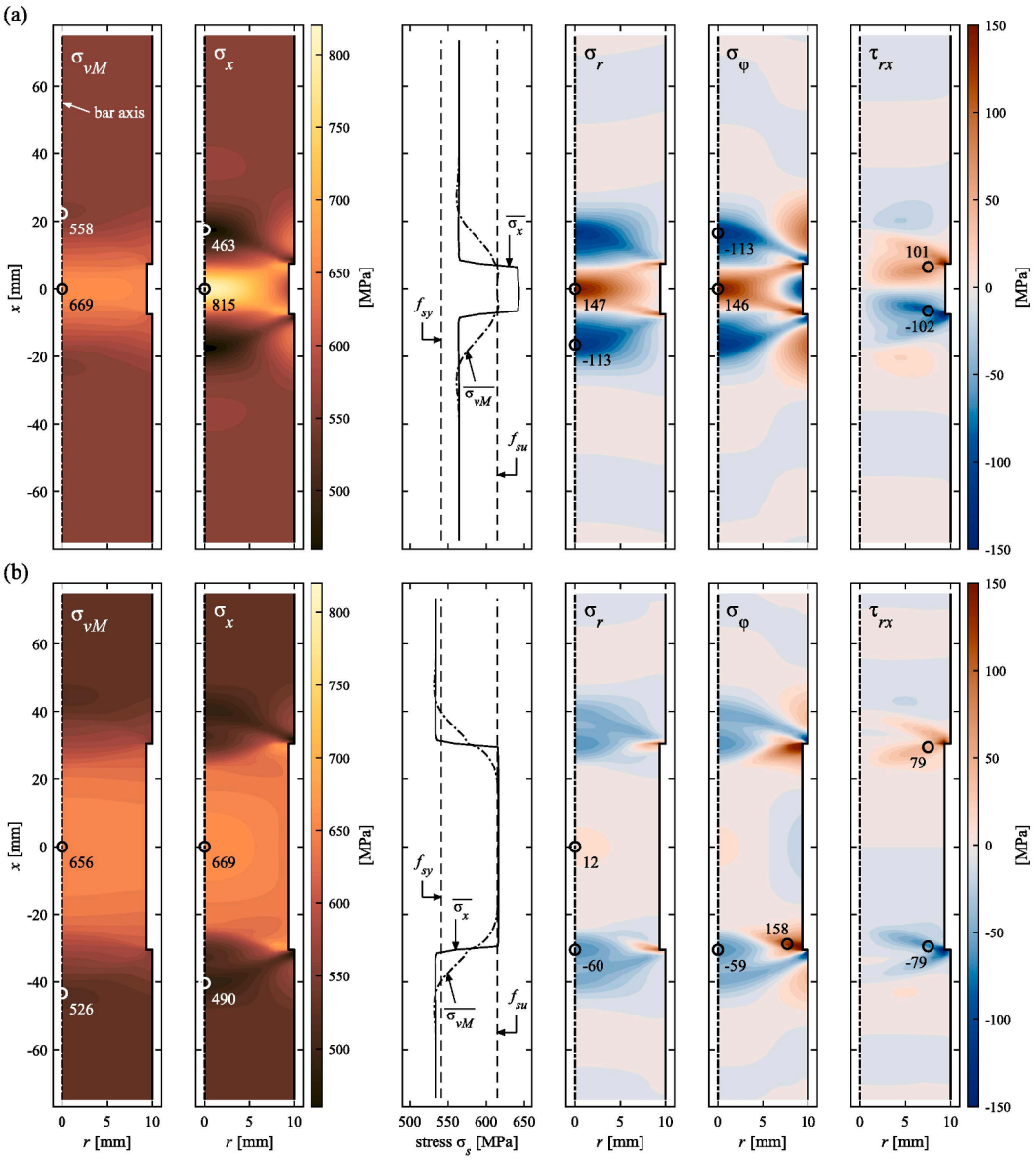

Fig. 8. Visualisation of triaxial stress state: Von Mises stress σ_{vM}, axial, radial and tangential stresses, σ_x, σ_r, and σ_φ, non-zero shear stresses τ_{rx}, and axial and von Mises stresses averaged over cross-section (Equation (11)) for (a) CW-15 and (b) CW-61. Locations of maximum and minimum stress are indicated with circles.

5.3. Analysis of the triaxial stress state

Fig. 8 illustrates the stress state for Specimens (a) CW-15 and (b) CW-61 at the peak load, showing the engineering values of the von Mises stress $\sigma_{vM}(r,x)$, the axial, radial, and tangential stresses, $\sigma_x(r,x)$, $\sigma_r(r,x)$, and $\sigma_\varphi(r,x)$, the non-zero shear stress $\tau_{rx}(r,x)$, and the distribution of the axial and von Mises stresses averaged over the cross-section, i.e.,

$$\overline{\sigma_x}(x) = \frac{\int_A \sigma_x(r,x)dA}{A}$$
$$\overline{\sigma_{vM}}(x) = \frac{\int_A \sigma_{vM}(r,x)dA}{A} \tag{11}$$
$$A = \begin{cases} A_{s,c} \text{ in damage zone} \\ A_s \text{ elsewhere} \end{cases}$$

The results are shown for a section between the bar axis and the bar surface in cylindrical coordinates. The maximum and minimum stress and the corresponding location are indicated per stress variable with a circle (at the cross-section transition, a small distance from the edge was chosen to avoid reporting potential singularities related to the FE mesh). Since the problem is axially symmetric and only a tensile force is applied, stresses do not depend on the rotation angle φ in the $r\varphi$-plane perpendicular to the x-axis, and the shear stresses in φ-direction vanish, $\tau_{r\varphi} = \tau_{x\varphi} = 0$. Hence, the von Mises stress simplifies to

$$\sigma_{vM} = \sqrt{\frac{1}{2}\left((\sigma_x - \sigma_r)^2 + (\sigma_r - \sigma_\varphi)^2 + (\sigma_\varphi - \sigma_x)^2\right) + 6\tau_{rx}^2} \tag{12}$$

The von Mises stresses $\sigma_{vM}(r,x)$ are similar for both specimens, with the maximum value in the range of the material tensile strength f_{su} = 615 MPa occurring at the centre of the damage zone. While they are fairly constant along the damage length, the von Mises stresses start decreasing near the cross-section transition, tending to a constant value (over both the cross-section and along the axis) at a distance ⩾1∅ away from the damage zone, where the stress state is essentially uniaxial. At

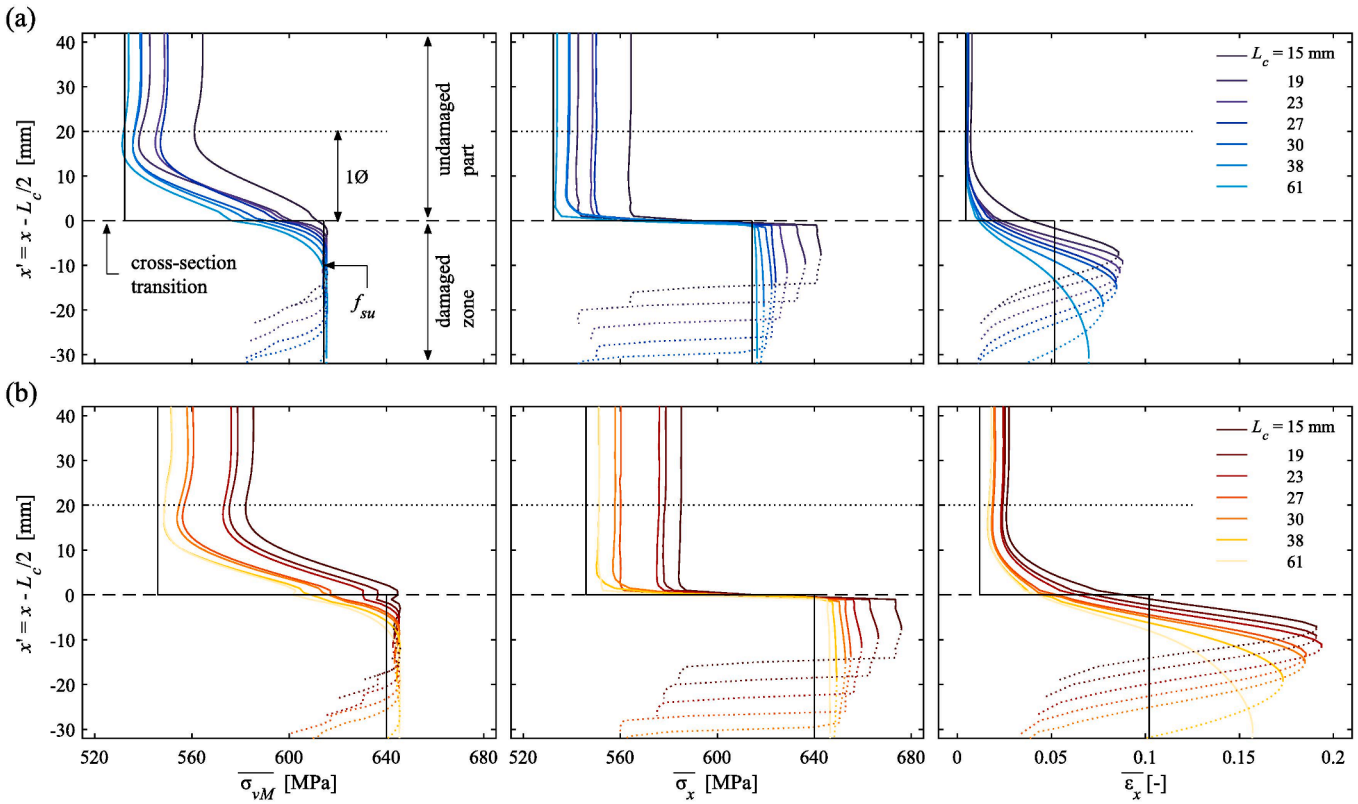

Fig. 9. Influence of triaxial stress state on the mean von Mises and mean axial stress $\overline{\sigma_{vM}}(x)$ and $\overline{\sigma_x}(x)$, and the mean axial strain over cross-section $\overline{\varepsilon_x}(x)$ for (a) the CW and (b) the QST reinforcement.

the centre of the damage zone ($x = 0$), the von Mises stress is approximately constant over the cross-section for CW-61, whereas it decreases towards the bar surface for CW-15.

The occurrence of a triaxial stress state within the damage zone (CW-15) or at its ends (CW-61) can easily be seen from the radial and tangential stresses, $\sigma_r(r,x)$ and $\sigma_\varphi(r,x)$. They are maximum near the cross-section transition, with a positive sign (tensile stresses) at the ends of the damage zone and a negative sign (compressive stresses) in the adjacent undamaged parts. The absolute shear stress (its value depends on the coordinate system) is highest at the edge of the cross-section transition, and decreases radially and axially. For a short damage length, the radial and tangential stresses are much higher than for a long damage length and extend over the entire damage zone, whereas an essentially uniaxial stress state is reached at the centre of a long damage length. Considering the considerable radial and tangential tensile stresses at $x = 0$ and Equation (12), it is evident that the axial stress can be substantially increased for a short damage length until the von Mises stress reaches the material uniaxial tensile stress. In contrast, no such increase is possible at the centre of a long damage length, where the axial stress approximately equals the von Mises stress.

At the peak load, the von Mises stress averaged over the cross-section (Equation (11)) exactly reaches the material uniaxial tensile strength for both specimens. This is noteworthy since the input material curve was not limited to the material tensile strength. This result indicates an excellent model accuracy since the von Mises stress is the representative value for comparing a triaxial stress state with uniaxial steel characteristics.

For CW-61, the mean axial stress at $x = 0$, coinciding with the von Mises stress, evidently also reaches the tensile strength and remains fairly constant over the entire damage length. At the cross-section transition, the mean axial stress drops sharply, whereas a gradual decrease is obtained for the von Mises stress in this zone. Both stress values are slightly below the uniaxial yield stress in the undamaged part, reaching a tensile stress of 534 MPa. This value can be validated by Equation (4), i.e., $\sigma_{s,uc} = \sigma_{s,c}(1-\zeta) = 533$ MPa (with $\sigma_{s,c} = f_{su} = 615$ MPa, and $\zeta = 0.133$ according to Table 1).

In the damage zone of CW-15, the mean axial stress reaches a peak value of 643 MPa, which is 4.5% higher than the uniaxial tensile strength (coinciding with the von Mises stress). This result matches well with the experiment, where an increase in peak stress of 3.5% was observed compared to the uniaxial tensile strength. As for CW-61, the mean axial stress drops sharply at the ends of the damage zone, whereas the von Mises stress gradually decreases over a length of approximately 1∅ from the damage zone end. Both stresses reach a value of 564 MPa in the undamaged part in the FE analysis, which corresponds well to the 565 MPa obtained from Equation (4) ($\sigma_{s,c} = 642$ MPa and $\zeta = 0.121$).

The FE analyses thus confirm the presence of a triaxial stress state near corrosion pits and underline its significant influence on the apparent uniaxial tensile strength of bars containing a short damage length, as it enables the activation of axial stresses exceeding the uniaxial tensile strength of the material. For long damage lengths, a uniaxial stress state is again reached at the centre of the damage zone, with conditions equal to those in a standard tensile test, and the apparent uniaxial peak stress cannot exceed the uniaxial tensile strength of the material. The influence of the triaxial stress state on the deformation behaviour is analysed in Section 5.4, and Section 6 explores for which damage geometries triaxial stresses potentially develop.

5.4. *Influence of a triaxial stress state on stresses and deformations*

The left two columns of Fig. 9 shows the mean von Mises and mean axial stresses according to Equation (11) at the peak load along the bar obtained from the FE analyses simulating (a) the CW series and (b) the QST series. The black lines indicate the uniaxial tensile strength from the material tests (shown in the damaged part) and the corresponding theoretical, reduced stress in the undamaged part (determined from

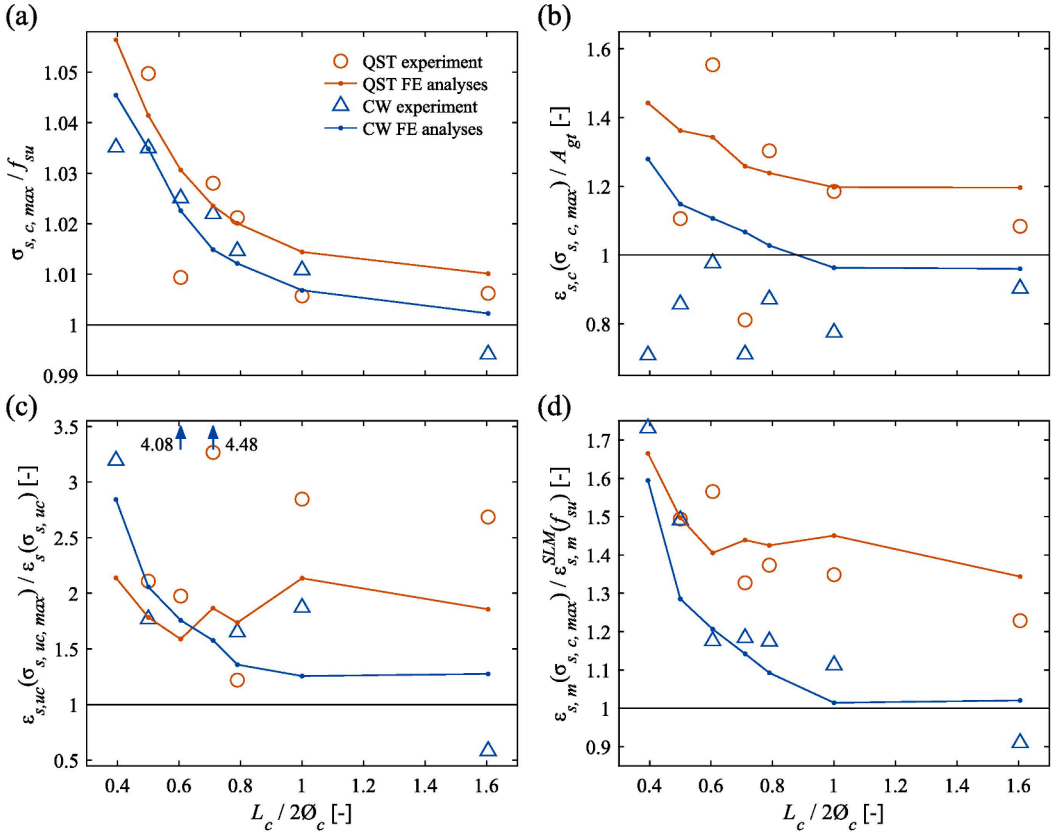

Fig. 10. Influence of triaxial stress state on peak stress and deformation, depending on damage length: (a) peak stress normalised by uniaxial material tensile strength; (b) strain in damage zone at peak stress, normalised with strain at peak stress of material tensile tests; (c) mean strain in adjacent undamaged part at peak stress, measured over a distance of one diameter from the cross-section transition, normalised with strain corresponding to a stress $\sigma_{s,uc} = (1-\zeta)f_{su}$ (Equation (4); positions of outlying values are indicated with arrows); (d) strain of Gauge GO (Fig. 3) at peak stress, normalised by strain according to SLM.

Equation (4)) as reference values. The plots in the right column of Fig. 9 show the mean axial engineering strains over the cross-section $\overline{\varepsilon_x}(x)$, along with the strain at the peak stress of the material tests in the damaged part and the corresponding theoretical value in the undamaged part as reference (black lines). Results are shown for only half of the modelled reinforcing bar (with the symmetry axis laying in the middle of the damage zones), and continuation is indicated with dotted lines. Note that a different coordinate is used along the bar axis than in Fig. 8, $x' = x - L_c/2$, i.e., the cross-section transition is positioned at $x' = 0$, which facilitates the comparison between the different damage lengths.

For all damage lengths, the mean von Mises stress in the damages zone exactly matches the uniaxial tensile strength for the CW series and is in good agreement for the QST series (indicating a slightly weaker FE model accuracy for the QST series). In the adjacent undamaged part, the stress decreases and reaches a constant value at a distance approximately 1∅ away from the damage zone, independently of the damage length. This is noteworthy since the peak load of the specimens increases with decreasing damage length, as indicated by the von Mises stresses at $x = 40$ mm, and confirms the principle of de Saint-Venant, stating that stress discontinuities generally attenuate over a length equal to the element width.

The mean axial stresses in the damage zone, hence the peak load, decrease with increasing damage length, reducing to the uniaxial material tensile strength for the damage lengths $L_c = 38$ and 61 mm (again almost exactly for the CW series and in good agreement for the QST series). Unlike for the von Mises stresses, there is a pronounced stress decrease at the cross-section transition, $x' = 0$. Nevertheless, the axial stress in the undamaged part equals the corresponding von Mises stress at a distance > 1∅ from the damage zone.

The mean strain starts to increase in the undamaged part at a distance of approximately 0.5…1.0∅ from the cross-section transition and reaches its maximum at the centre of the damage zone. The maximum strains are much higher than observed in the material tests, $\overline{\varepsilon_{x,max}} \approx 2A_{gt}$ for $L_c = 15$ mm and $\overline{\varepsilon_{x,max}} = 1.5A_{gt}$ for $L_c = 61$ mm. However, with increasing damage length, the mean strain is lower than A_{gt} over a considerable length at the ends of the damage zone, partly compensating the high maximum strain at the centre. On the other hand, as mentioned above, the mean strain in the undamaged part is higher than the expected theoretical strain over a length of 0.5…1.0∅ from the damage zone; hence the bar exhibits additional deformation in this region. Further away from the damage zone, the mean strain for specimens with long damage length equals the expected theoretical value, while it is higher for shorter damage lengths due to the increased peak load (compare the increased mean axial stresses). This strain increase is more pronounced for the QST bars due to the different shape of the stress–strain curve.

Fig. 10 compares the experimental results (markers) with the FE analyses (solid lines) at the peak load, plotting them against the normalised damage length: (a) peak stress in the damage zone, (b) mean strain over the damage zone, (c) mean strain over the first 20 mm in the undamaged part adjacent to the cross-section transition (between $0 \leqslant x' \leqslant$ 20 mm in Fig. 9), and (d) mean strain at the Gauge GO extending over the damage zone and the undamaged part, as shown in Fig. 3. The results are normalised with their corresponding theoretical values (f_{su}, A_{gt}, $\varepsilon_s(\sigma_{s,uc} = (1-\zeta)f_{su})$, and $\varepsilon_{s,m}^{SLM}(\sigma_{s,c} = f_{su})$ according to the SLM and Equation (6)). Note that the experimental results in Fig. 10 (a) and (d) correspond to those in Fig. 4 (a) and (b).

The results of the FE analyses match the experimentally observed

increased peak stresses very well, for the CW as well as the QST bars, see Fig. 10 (a). Regarding the mean strain over the damage length (Fig. 10 (b)), the FE analyses predict the experimental results of the QST bars fairly well, particularly compared to the conventional prediction (=A_{gt}), which underestimates the experimentally observed mean strain in the damage zone by up to 40%. The experimentally observed strains for the CW series do not show a clear tendency regarding damage length, but all strains are below A_{gt}. The FE analyses predict strains slightly lower than A_{gt} for long damage lengths, but a moderate increase for shorter damage lengths. The mismatch might be due to a model inaccuracy or secondary effects having influenced the strain measurements in the experiments (influence of ribs, presence of bending stresses caused by a slight shift of the centroidal axis due to tolerances when reducing the diameter).

The experimentally observed mean strains measured over the first 20 mm (1Ø) of the undamaged part (Fig. 10 (c)) – which are strongly underestimated by the SLM (roughly 20% for long damage lengths and up to a factor of 3 for short damage lengths) – are fairly well predicted by the FE analyses for both, the CW and the QST reinforcement. However, the large scatter of the experimental results reflects the challenge of accurately measuring strains in reinforcing bars over a short reference length, even with advanced measurement technologies.

Fig. 10 (d) shows the experimentally measured, normalised mean strain in Gauge GO of Fig. 3 and the corresponding results of the FE analyses. The FE analyses match the experimental data accurately for the CW reinforcement and slightly overpredicts the results for the QST reinforcement. The experimental results as well as the FE analyses indicate that for damage lengths shorter than twice the reduced diameter, i.e., $L_c \leqslant 2\varnothing_c$, the SLM tends to strongly underestimate the deformation capacity of damaged reinforcing bars by 10…70% in the cases investigated here. This is due to the beneficial effects of the triaxial stress state at the cross-section transition, which partly compensates the strain localisation effect described by the SLM (Equation (6)).

5.5. Influence of a triaxial stress state on the yield behaviour

The strain measurements of gauges near the cross-section transition of QST bars illustrated in Fig. 6 revealed (i) a reduced yield stress and (ii) a loss of the yield plateau (see Section 4.3). The yield stress increased again further away from the damage zone, and a yield plateau was retrieved. Both effects directly result from the triaxial stress state near the cross-section transition.

The apparently reduced yield stress in the undamaged part adjoining the damaged zone follows from the distribution of the von Mises stresses $\overline{\sigma_{vM}}$ in Fig. 8 (b), where the von Mises yield criterion $\overline{\sigma_{vM}} = f_{sy}$ is reached or exceeded for $30 \leqslant |x| \leqslant 40$ mm, and hence, yielding occurs, whereas the mean axial stress is still below the yield stress, i.e., $\overline{\sigma_x} = 534$ MPa $< f_{sy}$. In contrast, if one scales the mean von Mises and mean axial stress distributions in Fig. 8 (a), it evolves that a stress state $\overline{\sigma_{vM}} \leqslant f_{sy} < \overline{\sigma_x}$ exists where no plastic deformations occur in the damaged part, although the mean axial stresses exceed the yield stress. Hence, the apparent yield stress is increased.

The macroscopic occurrence of a yield plateau in low carbon steel is related to the formation of Lüders bands, i.e., discrete local bands of high deformation increase (discontinuous yielding) due to a sudden break free of the dislocations from the interstitial carbon atoms (Cottrell-Bilby clouds), which propagate along the reinforcing bar (see, e.g., [41–46]). It has been shown that the Lüders band front orients in the direction of the maximum shear stress (i.e., 45° to the bar axis for pure tension) [42,46]. The presence of shear stresses τ_{xr} at the cross-section transition (see Fig. 8) causes the stress trajectories to rotate, leading to a variation of the maximum shear stress direction over the cross-section. This could hinder the Lüders bands from propagating in an ordered manner [47]. Moreover, it is probable that the varying von Mises stress (which represents the yield criterion) over the cross-section triggers the dislocations to break free from their interstitial atoms in only a few grains simultaneously. This hypothesis is supported by the fact that in the FE analyses simulating bars with short damage lengths – for which a wide range of stress values is exhibited over the cross-section, see Fig. 8 – no yield plateau was obtained either (see curves for $L_c/2\varnothing_c = 0.2$ in Fig. 11 (b)). Hence, these issues presumably hinder the occurrence of macroscopically visible Lüders bands (i.e., a yield plateau) and favour continuous yielding with strain hardening near the cross-section transition, as also observed in a recent study in the context of bond [47].

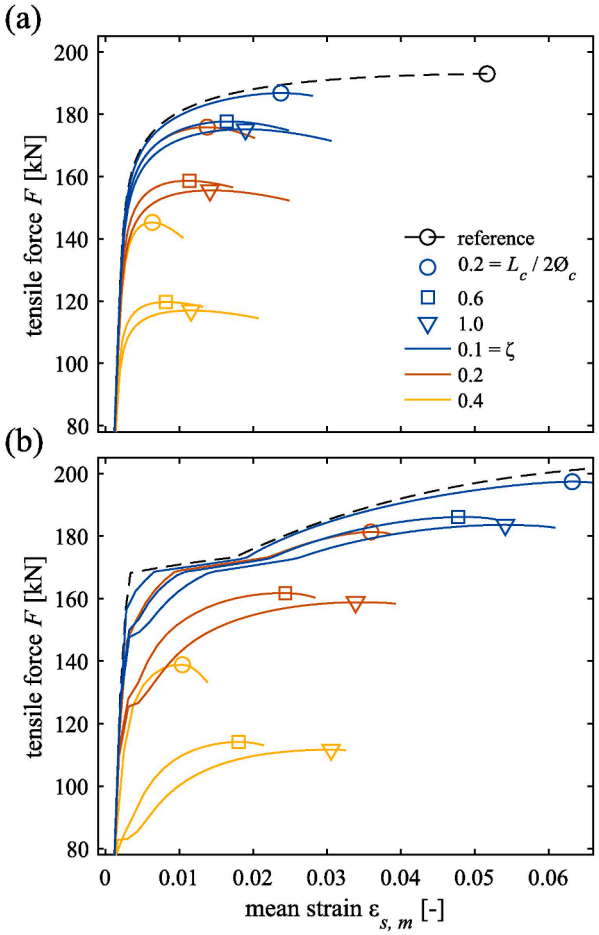

Fig. 11. Selected force-mean strain curves of parametric study to illustrate the strong influence of a triaxial stress state, depending on damage length $L_c/(2\varnothing_c)$ and cross-section loss ζ, for (a) CW and (b) QST reinforcement.

6. Parametric study

6.1. Aim and setup

Besides the material characteristics, the formation of a triaxial stress state is mainly governed by the diameter of the residual cross-section $\varnothing_c$ and the length of the damage zone L_c. To investigate the influence of these parameters on the triaxial stress state, a parametric study was conducted, investigating the force–elongation behaviour of a reinforcing bar with a total length $L_{tot} = 150$ mm and exhibiting a cross-section loss $\zeta = 0.05...0.8$ over a variable length $L_c/(2\varnothing_c) = 0.2...1.4$. The bar behaviour was simulated using the FE model described in Section 5.1 and adopting the two material models of Section 3.2. The initial diameter was held constant at $\varnothing = 20$ mm, yielding $\varnothing_c = 8.95...19.5$ mm and $L_c = 3.6...54.6$ mm. By normalising with $\varnothing_c/\varnothing$, $\varnothing_c^2/\varnothing^2$, and $L_c/2\varnothing_c$, respectively, the results apply to other bar and damage geometries within the limitation set in this paper, i.e., an axisymmetric cross-section

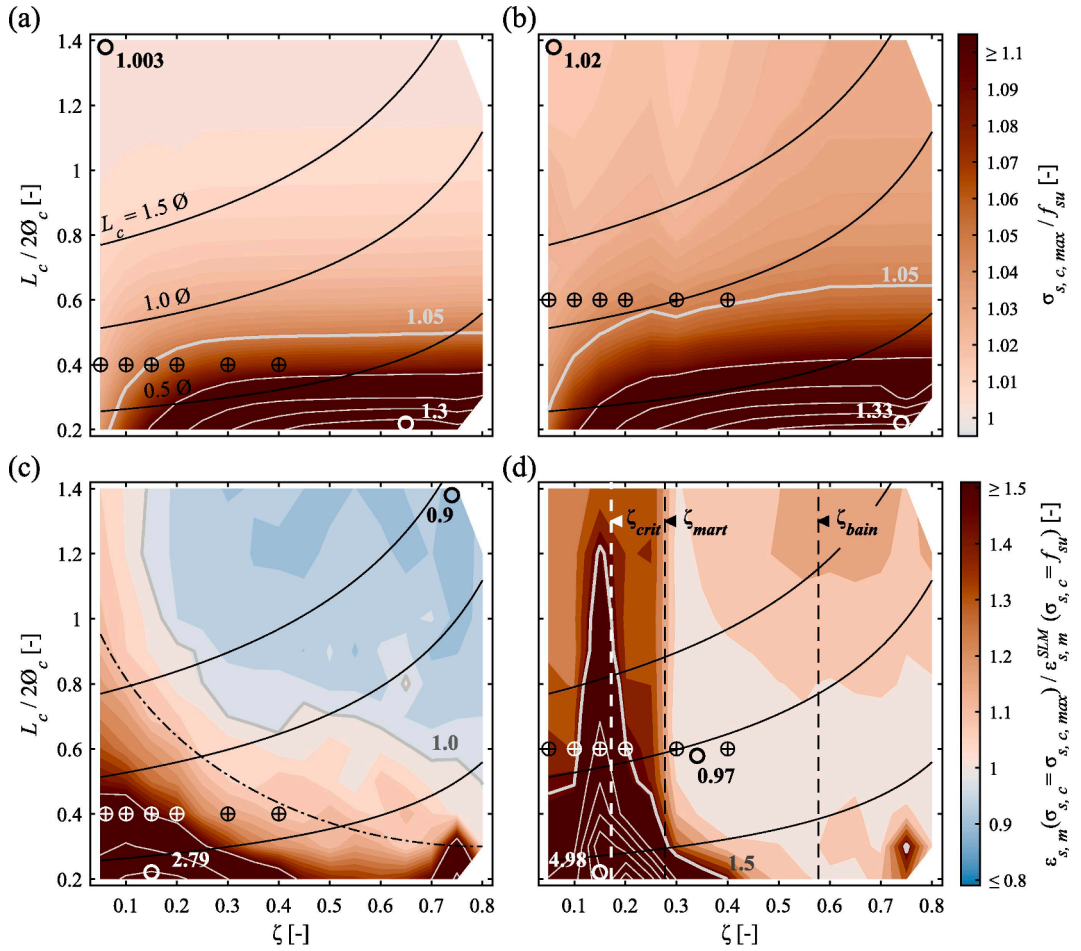

Fig. 12. Load-carrying and deformation capacity predicted by the FE analyses compared to the uniaxial tensile strength and the SLM. (a), (b) ratios of the peak stress (FE) to the uniaxial material tensile strength for CW and QST bars, respectively. (c), (d) ratios of strain at peak stress of the FE analyses to that of the SLM for CW and QST bars, respectively. Solid black lines correspond to constant damage lengths, circular markers show extreme values, and target markers correspond to the parameter sets analysed in Fig. 13. Isolines are plotted in grey, with an equidistance of 0.05 in (a, b) and 0.5 in (c, d).

reduction. A total number of 544 simulations (272 per steel type) were run and evaluated.

6.2. General results

As an overview, Fig. 11 shows selected force - mean strain curves resulting from the parametric study for (a) CW and (b) QST reinforcing bars with different damage lengths ($L_c/(2Ø_c)$=0.2, 0.6, and 1.0, indicated with different markers) and different cross-section losses (ζ=0.1, 0.2, and 0.4, indicated with different colours). The stress–strain curves of the undamaged bars are shown in black as a reference.

As expected, the peak load generally decreases with increasing cross-section loss. However, for a specific cross-section loss, it varies considerably and increases with decreasing damage length. Similar to the maximum load, the strain at peak stress generally decreases with increasing cross-section loss. However, the results indicate that the peak strain for a short damage length (circular markers) can even be larger than for a longer damage length (square and triangular markers) for small or moderate cross-section loss (blue and red curves). This result contradicts the SLM (Equation (6)) and is caused by the triaxial stress state.

6.3. Load-carrying and deformation capacity compared to the SLM

Fig. 12 (a) and (b) show contour plots of the ratio $\sigma_{s,c,max}/f_{su}$, i.e., the deviation of the peak stress obtained by the FE analyses from the uniaxial material tensile strength, for (a) the CW and (b) the QST reinforcing steel. Results are shown in the parameter range of the cross-section loss ζ and the normalised damage length $L_c/(2Ø_c)$ as defined in Section 6.1. Red colours indicate an underestimation of the peak load; note that the colour map is limited to $1.1f_{su}$ for a higher resolution in the main part of the diagram. The maximum and minimum values and their locations are indicated with circles. Black lines indicate constant normalised damage lengths L_c; they are curved because the residual bar diameter $Ø_c$ and thus the ratio $L_c/(2Ø_c)$ constantly vary with the cross-section loss ζ. Isolines are plotted in grey, with an equidistance of 0.05 in (a) and(b), and 0.5 in (c) and (d).

For damage lengths longer than 1Ø, the load-carrying capacity is underestimated by less than 5% for both steel types, almost independently of the cross-section loss. The load-carrying capacity is underestimated by 5…10% for damage lengths in the range of 0.5Ø to 1Ø, and by 10…35% for shorter damage lengths.

Fig. 12 (c) and (d) show contour plots of the strain ratio $\varepsilon_{s,m}(\sigma_{s,c,max})/\varepsilon^{SLM}_{s,m}(\sigma_{s,c} = f_{su})$, i.e., the deviation of the strain at peak load obtained by the FE analyses from the strain at peak load according to the SLM (Equation (6)), for (c) the CW and (d) the QST reinforcing steel. Red colours indicate an underestimation of the strain at peak stress by the SLM, and blue colours an overestimation. Note that the colour map is limited to 0.8 and 1.5 for a higher resolution of the main part of the diagram. The dashed line in Fig. 12 (d) indicates the critical cross-section loss ζ_{crit}, denoting the maximum cross-section loss for which the undamaged cross-section still reaches the yield stress at maximum load according to the SLM (see [13]). Additionally, the cross-section loss

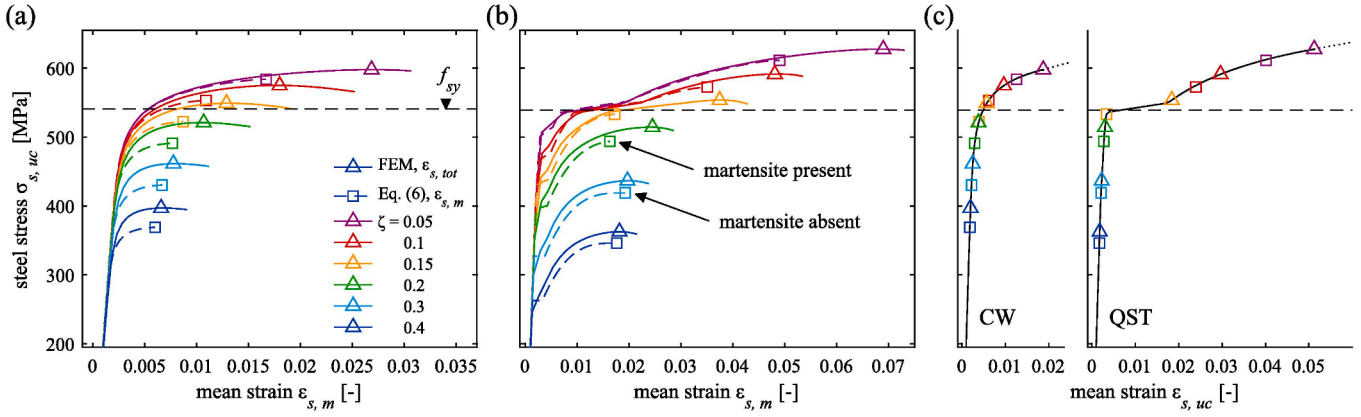

Fig. 13. Stress-mean strain diagrams for the damage conditions indicated with black markers in Fig. 12 for (a) the CW and (b) the QST reinforcement. Solid lines correspond to the FE analyses, and dashed lines to the SLM; (c) peak stresses and corresponding strains of FE analyses (traingles) and SLM (squares) in the undamaged part far away from the damage zone together with the constitutive material relationships (black) for validation. All stresses refer to the initial cross-sectional area.

ζ_{mart} indicates the complete loss of the martensitic outer annulus for the QST bar, and ζ_{bain} indicates the complete loss of the bainitic transition zone (see [31]).

For the CW reinforcing steel in Fig. 12 (c) and the chosen parameter range, an empirical, elliptical relationship was found, above which the error made by using an SLM is less than ± 10%:

$$R(\zeta, L_c) = \left(\frac{\zeta}{0.8} - 1\right)^2 + \left(\frac{L_c}{2\varnothing\sqrt{1-\zeta}} - 1.3\right)^2 \leqslant 1 \tag{13}$$

The limit $R(\zeta, L_c) = 1.0$ is shown in Fig. 12 (c) with a dash-dotted line. For shorter damage lengths and smaller cross-section losses, the SLM underestimates the deformation capacity, especially for $\zeta < 0.4$ and $L_c/(2\varnothing_c) < 0.4$, where the peak strain ratio reaches a maximum value of $\varepsilon_{s,m}/\varepsilon_{s,m}^{SLM} = 2.8$.

For QST reinforcing bars, Fig. 12 (d) indicates that the underestimation of the deformation capacity by the SLM is acceptable, i.e., $\varepsilon_{s,m}/\varepsilon_{s,m}^{SLM} < 1.2$, for cross-section losses $\zeta > \zeta_{mart}$ (and $L_c/(2\varnothing_c) > 0.3$); this might be an artefact of the constitutive material model formulated in [31], with an increase of the strain at peak stress as soon as the martensitic outer annulus is completely lost. Independent of the damage length, the SLM underestimates the deformation capacity most pronouncedly around the critical cross-section loss ζ_{crit}, with a maximum ratio $\varepsilon_{s,m}/\varepsilon_{s,m}^{SLM} \approx 5$ for short damage lengths $L_c \leqslant \varnothing$, and peak strain ratios greater than 1.5 even for long damage lengths.

Fig. 13 (a) and (b) show the stress-mean strain diagrams for the simulated CW bars with $L_c/(2\varnothing_c) = 0.4$, and QST bars with $L_c/(2\varnothing_c) = 0.6$, respectively, for cross-section losses $\zeta = 0.05...0.4$. These damage conditions (parameters $(\zeta|L_c/(2\varnothing_c))$) are depicted with target markers in Fig. 12. Solid lines show the behaviour obtained from the FE analyses, and dashed lines show the predictions according to the SLM (Equation (6)), with triangular (FE) and square (SLM) markers indicating the peak stress and corresponding strain. The stress is related to the undamaged, initial cross-sectional area A_s (Equation (2)). Fig. 13 (c) shows the constitutive material relationships (black lines) and the stresses and strains observed in the undamaged parts (far away from the damage zone) at the peak forces of the calculations shown in Fig. 13 (a) and (b).

Fig. 13 (a) and (b) show a significantly decreasing load-carrying capacity with increasing damage, and a substantial decrease in deformation capacity already for low cross-section losses. This is a direct consequence of the strain localisation described in Section 1.1. The concept of the critical cross-section loss [13] explains why the deformation capacity is almost entirely lost as soon as the stress in the undamaged part drops below the yield stress.

For the CW bars, Fig. 13 (a) and (c) show that the difference in the mean strain at peak stress between the FE analyses and the SLM is highest for low cross-section losses $\zeta < \zeta_{crit}$, where the undamaged part of the bar also exhibits significant plastic strains. Since load variations in the plastic strain range can lead to significantly different strains, it is evident that the FE analyses, which unlike the SLM account for the increased maximum load due to the triaxial stress state, lead to significantly larger deformations than the SLM. As soon as the undamaged part

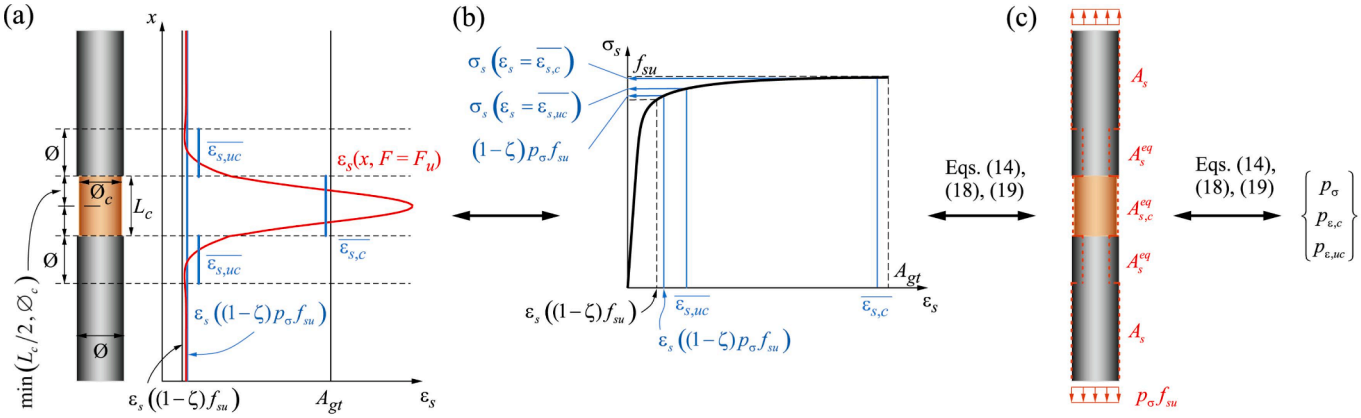

Fig. 14. Schematic representation of model strategy: (a) strain distribution at peak load (red) and mean strains in the vicinity of the cross-section transition according to Equations (15) and (16); (b) stresses resulting from material stress–strain curve for mean strains; (c) equivalent cross-sectional areas (red dotted lines) according to Equations (17) and (18). (For interpretation of the references to colour in this figure legend, the reader is referred to the web version of this article.)

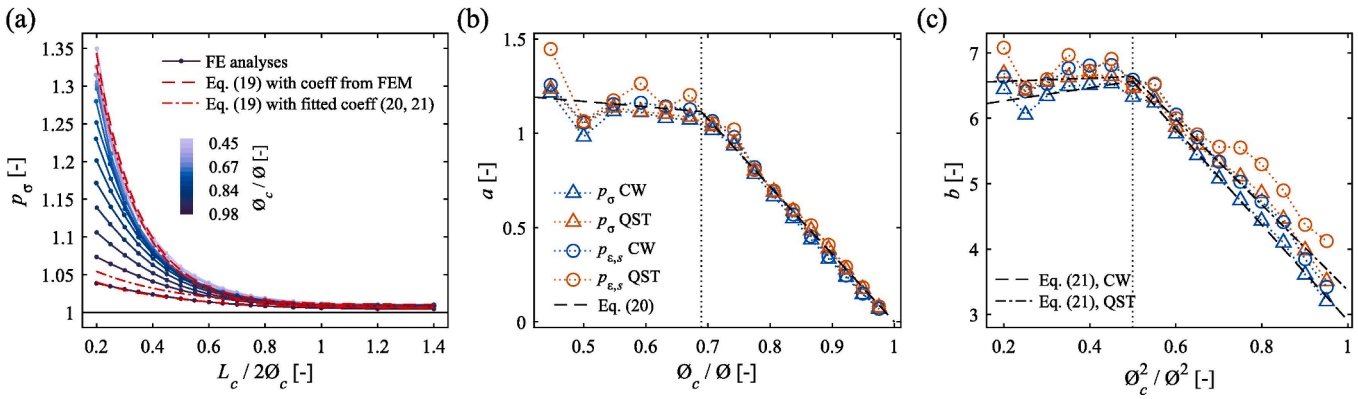

Fig. 15. Simplified model approximating the effects of the triaxial stress state: (a) parameter p_σ for the CW bars as a function of normalised damage length and diameter ratio (blue), and evaluation of Equation (19) (red). (b, c) regression parameters a and b, respectively, as functions of linear and squared diameter ratios (coloured), and fits according to Equations (20) and (21) (dashed and dash-dotted black lines). (For interpretation of the references to colour in this figure legend, the reader is referred to the web version of this article.)

is not reaching the yield stress, the predicted strains at peak stress of both models start converging, although the predicted peak loads still differ significantly.

The same observations apply to the QST reinforcing bars, Fig. 13 (b) and (c), where again significant differences in strain at peak stress are observed for small cross-section losses, i.e., where the undamaged part also exhibits plastic strains, with the largest difference between the two models occurring for $\zeta = 0.2$. For this cross-section loss, the undamaged part reaches strains at the onset of hardening in the FE analyses (accounting for a higher peak load due to the triaxial stress state), whereas the strains according to the SLM – with a 4% lower maximum load – are just below the elastic limit (yield point). The FE- and SLM-strains in the undamaged zone thus differ by the length of the yield plateau (Lüders strain, see Fig. 13 (c)). This explains the considerable differences (i.e., the high ratios) observed in Fig. 12 (d) for QST bars with a cross-section loss $\zeta \approx \zeta_{crit}$, irrespective of the damage length. Moreover, the loss of the martensitic outer annulus for $\zeta > 0.28$ has a visible influence on the differences between the model predictions, as can be seen from Fig. 13 (b).

7. Simplified modelling approach to estimate the influence of the triaxial stress state

While FE analyses of reinforcing bars with local damage are well suited to investigate and explain the effects of a triaxial stress state, modelling entire concrete structures containing locally corroded reinforcement on such a level of detail is not expedient, particularly due to the immense computational effort. Hence, simplified models are needed to capture the governing effects with reasonable accuracy. Such a simplified approach is proposed in this section, valid for the parameter ranges set in Section 6.1 and following the model strategy illustrated in Fig. 14.

7.1. General model strategy

As seen in the previous sections, a shorter damage length leads to a considerable increase in the apparent uniaxial tensile strength $\sigma_{s,c,max}$ (Equation (1)), which is decisive for the differences between the FE analyses and the SLM. The effect is captured in the following by the parameter p_σ, defined as the ratio of the maximum apparent uniaxial stress and the material tensile strength:

$$p_\sigma = \frac{\sigma_{s,c,max}}{f_{su}} \tag{14}$$

The proposed approach is based on the observation that in all FE analyses, the triaxial stress state had a limited influence length, defined as the length between the cross-section transition and the point where $\overline{\sigma_{vM}}(x) \approx \overline{\sigma_x}(x)$ (see Figs. 8 and 9) and corresponding to $0.75...1.0\varnothing$ and $\min(L_c/2,\ 0.7...0.9\varnothing_c)$ for the undamaged and damaged parts, respectively.

The results of the FE analyses align well with the principle of de Saint-Venant, whose direct application would result in influence lengths of one diameter. For simplicity, this value is adopted in the following. The strains near the cross-section transition of the FE analyses were thus averaged over lengths of $1\varnothing$ and $\min(L_c/2,\ \varnothing_c)$ in the undamaged and damaged part, respectively, resulting in the following mean strains $\overline{\varepsilon_{s,c}}$ (damaged part) and $\overline{\varepsilon_{s,uc}}$ (undamaged part) at peak load $F = F_u$ (see Fig. 14):

$$\overline{\varepsilon_{s,c}} = \int_0^s \overline{\varepsilon_x}(x, F = F_u)dx \Big/ s \qquad s = \min(L_c/2,\ \varnothing_c) \tag{15}$$

$$\overline{\varepsilon_{s,uc}} = \int_{-\varnothing}^0 \overline{\varepsilon_x}(x, F = F_u)dx \Big/ \varnothing \tag{16}$$

The stresses corresponding to these mean strains are determined from the stress–strain diagram of the material tensile tests. By dividing the applied maximum force by these stresses, one gets the equivalent cross-sectional areas $A_{s,c}^{eq}$ and A_s^{eq}, i.e., the cross-sectional area of a fictitious bar exhibiting these mean strains at peak load (Fig. 14):

$$A_{s,c}^{eq} = \frac{F_u}{\sigma_s\left(\varepsilon_s = \overline{\varepsilon_{s,c}}\right)} = \frac{A_{s,c} f_{su} p_\sigma}{\sigma_s\left(\varepsilon_s = \overline{\varepsilon_{s,c}}\right)} \qquad p_{\varepsilon,c} = \frac{A_{s,c}^{eq}}{A_{s,c}} = \frac{f_{su} p_\sigma}{\sigma_s\left(\varepsilon_s = \overline{\varepsilon_{s,c}}\right)} \tag{17}$$

$$A_s^{eq} = \frac{F_u}{\sigma_s\left(\varepsilon_s = \overline{\varepsilon_{s,uc}}\right)} = \frac{A_{s,c} f_{su} p_\sigma}{\sigma_s\left(\varepsilon_s = \overline{\varepsilon_{s,uc}}\right)} \qquad p_{\varepsilon,uc} = \frac{A_s^{eq}}{A_s} = \frac{A_{s,c}}{A_s} \frac{f_{su} p_\sigma}{\sigma_s\left(\varepsilon_s = \overline{\varepsilon_{s,uc}}\right)} \tag{18}$$

The parameters $p_{\varepsilon,c}$ and $p_{\varepsilon,uc}$ are the ratios between the equivalent and the actual cross-sectional areas. The parameters p_σ, $p_{\varepsilon,c}$, and $p_{\varepsilon,uc}$ thus represent the effect of the triaxial stress state regarding peak stress and corresponding strain on the bar load-deformation behaviour, i.e., the differences compared to the SLM (Equation (6)). They were determined for every FE analysis and are analysed in the following section.

7.2. Model parameter evaluation

Fig. 15 (a) illustrates the parameters p_σ obtained for the CW bars with different ratios $\varnothing_c/\varnothing$ in blue, plotted vs the normalised damage length.

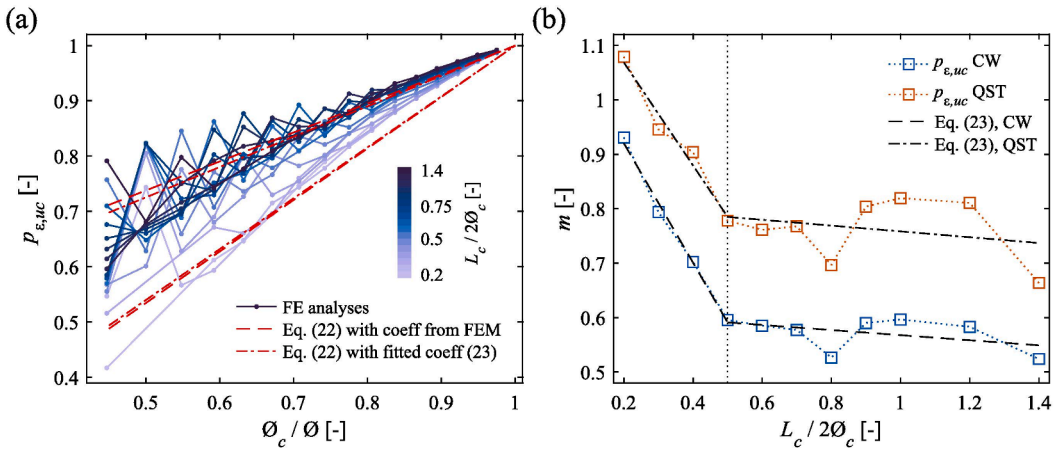

Fig. 16. Simplified model approximating the effects of the triaxial stress state: (a) parameter $p_{\varepsilon,uc}$ for the CW bars as a function of damage length and diameter ratio (blue), and evaluation of Equation (22) (red). (b) regression parameter m as a function of normalised damage length (coloured) and fits according to Equation (23) (dashed and dash-dotted black lines). (For interpretation of the references to colour in this figure legend, the reader is referred to the web version of this article.)

The peak stress increases strongly with decreasing damage length and residual diameter, while the influence of the triaxial stress state evidently vanishes at large damage lengths, with no increase in the peak stress for $L_c \geqslant (2Ø_c)$, irrespective of the residual diameter.

The FE analyses showed that the parameters p_σ and $p_{\varepsilon,c}$ are virtually identical, and there are only marginal differences between the CW and the QST bars despite the strongly differing steel characteristics. The distribution of both parameters, p_σ and $p_{\varepsilon,c}$, can thus be approximated by the same empirical relationship, valid for the CW and the QST bars:

$$p_\sigma = p_{\varepsilon,c} = a e^{-b(L_c/(2Ø_c))} + c \tag{19}$$

with a, b, c = fitting parameters depending on the diameter ratio $Ø_c/Ø$ and the steel type (CW or QST). The parameter c is set equal to unity for the CW bars, as expected for long damage lengths, and slightly higher ($c = 1.01$) to achieve a better fit for the QST bars. Fig. 15 (b) and (c) show the distribution of the parameters a and b, respectively, found by linear regression, as functions of $Ø_c/Ø$ and $(Ø_c/Ø)^2$, respectively, with triangles indicating the results for p_σ and circles those for $p_{\varepsilon,c}$. The parameters for the QST reinforcing steel are shown in blue, and those of the CW reinforcing steel in red. The virtually identical values of both parameters and reinforcing steel types is seen in both figures.

As a further simplification, the fitting parameter a is assumed to be bilinear in $Ø_c/Ø$, independent of the steel type:

$$a = \begin{cases} -0.3Ø_c/Ø + 1.3 & \text{for } Ø_c/Ø \leqslant 0.69 \\ -3.6Ø_c/Ø + 3.6 & \text{for } Ø_c/Ø > 0.69 \end{cases} \tag{20}$$

and the fitting parameter b is assumed to be bilinear in $Ø_c^2/Ø^2$, and slightly dependent on the steel type:

$$b(\text{CW}) = \begin{cases} 1.0Ø_c^2/Ø^2 + 6.1 & \text{for } Ø_c^2/Ø^2 \leqslant 0.5 \\ -7.3Ø_c^2/Ø^2 + 10.2 & \text{for } Ø_c^2/Ø^2 > 0.5 \end{cases} \tag{21}$$

where the fitting coefficients were again obtained by regression. Fig. 15 (a) includes the results obtained from Equation (19) as red lines for $Ø_c/Ø = 0.98$ ($\zeta = 0.05$) and $Ø_c/Ø = 0.45$ ($\zeta = 0.8$), once using the parameters a and b found by the linear regression of the FE analyses (i.e., the values indicated with red triangles in Fig. 15 (b) and (c)), and once using the bilinear parameters defined by Equations (20) and (21). Both parameter sets fit the results of the FE analyses almost equally well.

Fig. 16 (a) shows the parameter $p_{\varepsilon,uc}$ of the CW reinforcing steel in blue for different normalised damage lengths $L_c/(2Ø_c)$ vs the diameter ratio $Ø_c/Ø$. The curves are serrated for low $Ø_c/Ø$-ratios, i.e., high cross-section losses, most probably due to the chosen load steps in the FE analyses. For a specific damage length, $p_{\varepsilon,uc}$ increases with the residual diameter, i.e., as the residual cross-sectional area approximates the initial cross-sectional area, and the influence of the triaxial stress state in the adjacent undamaged parts reduces. Similarly, $p_{\varepsilon,uc}$ increases with the damage length, but only up to $L_c = Ø_c$ beyond which it is independent of L_c. This observation indicates that the damage length influences the triaxial stress state in the adjacent undamaged part much less than the cross-section loss.

The parameter $p_{\varepsilon,uc}$ was found to be roughly proportional to the diameter ratio, and can thus be approximated by a straight line with the slope m

$$p_{\varepsilon,uc} = m(Ø_c/Ø - 1) + 1 \tag{22}$$

Fig. 16 (b) shows the slopes obtained by linear regression of the FE

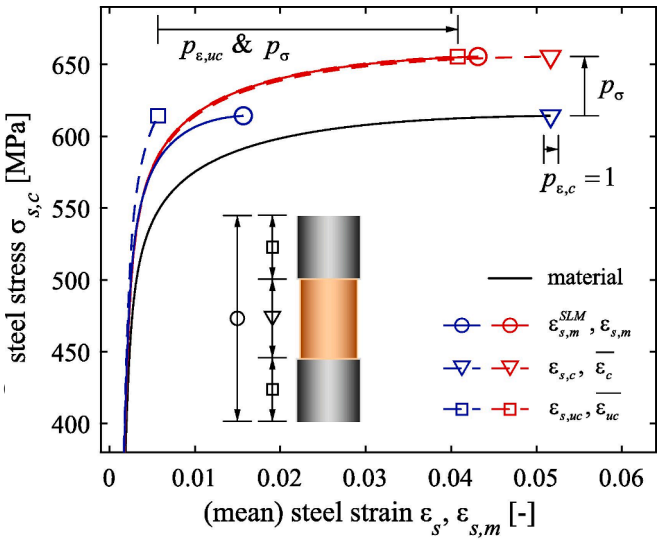

Fig. 17. Comparison of material stress–strain relationship (black), stress-mean strain relationship over the length $L_{tot} = L_c + 2Ø$ according to the SLM (Equation (6)), blue) and the simplified modelling approach accounting for the triaxial stress state (red). Example for $Ø = 18$ mm, $Ø_c = 17$ mm, $L_c = 10$ mm, and constitutive material relationship defined in Equation (5). (For interpretation of the references to colour in this figure legend, the reader is referred to the web version of this article.)

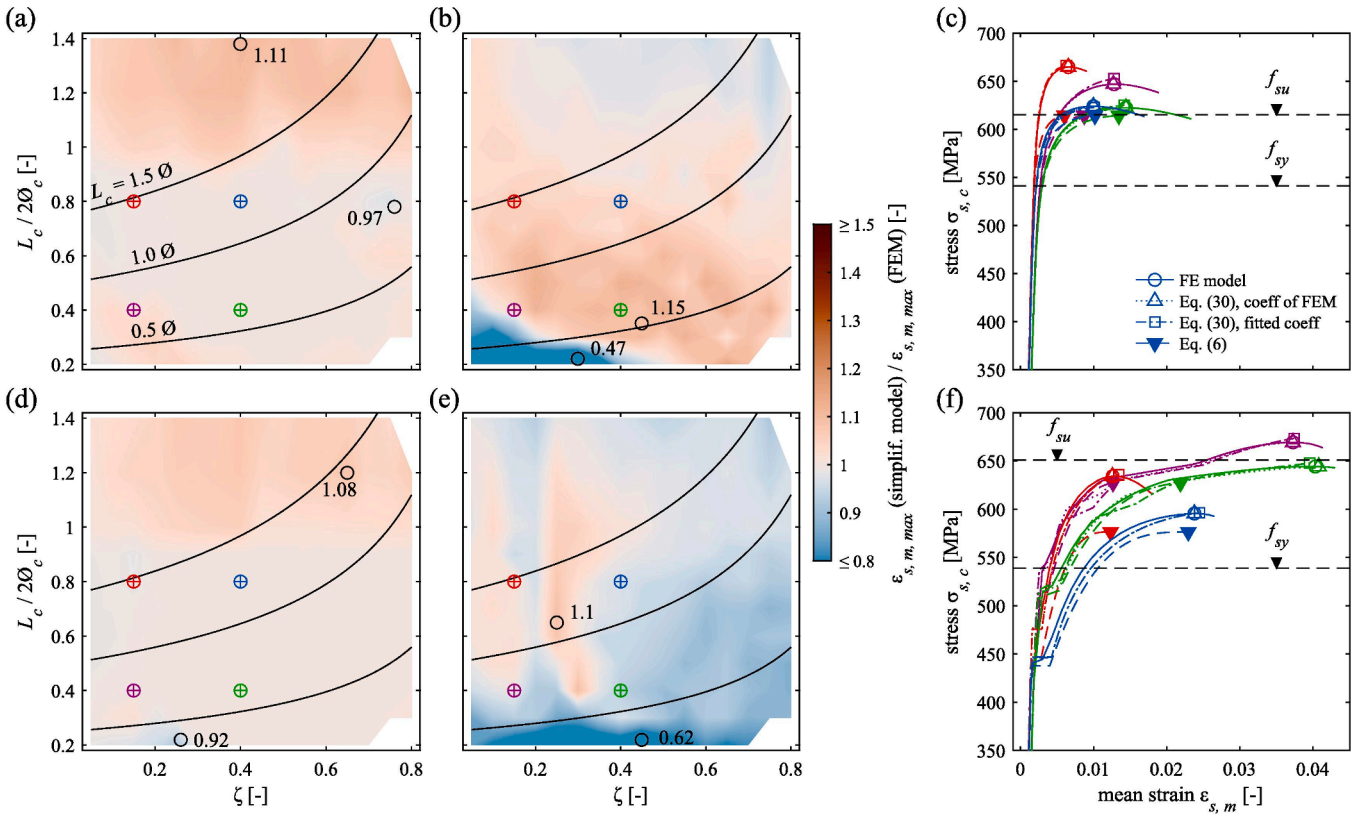

Fig. 18. Comparison of the strain at peak stress predicted by the FE analyses and the simplified model of Sections 7.2 and 7.3 for (a, b) CW and (d, e) QST bars. For (a, d), model coefficients for the simplified model were chosen according to the FE analyses; for (b, e) coefficients were chosen according to Equations (20), (21), and (23). (c, f) stress-mean strain curves of the FE analyses, the simplified model and the SLM at the points indicated with target markers in (a, b, d, e).

analyses shown in Fig. 16 (a) (blue = CW bars, red = QST bars). The parameter m strongly depends on the type of reinforcing steel, with the QST steel showing higher values than the CW steel, indicating a stronger influence of the triaxial stress state. The slope stays approximately constant for $L_c > \varnothing_c$, i.e., the parameter $p_{\varepsilon,uc}$ merely depends on the diameter ratio, except for very short damage lengths.

The parameter m is assumed to be bilinear in $L_c/(2\varnothing_c)$, hence one gets by regression:

$$m(\mathrm{CW}) \approx \begin{cases} -1.10(L_c/2\varnothing_c) + 1.14 & \text{for } L_c/2\varnothing_c \leqslant 0.5 \\ -0.05(L_c/2\varnothing_c) + 0.62 & \text{for } L_c/2\varnothing_c > 0.5 \end{cases}$$
$$m(\mathrm{QST}) \approx \begin{cases} -0.95(L_c/2\varnothing_c) + 1.26 & \text{for } L_c/2\varnothing_c \leqslant 0.5 \\ -0.05(L_c/2\varnothing_c) + 0.81 & \text{for } L_c/2\varnothing_c > 0.5 \end{cases} \quad (23)$$

Fig. 16 (a) shows the results of Equation (22) as red lines for $L_c/\varnothing_c = 0.2$ and $L_c/\varnothing_c = 1.4$. The dashed lines are obtained for the parameter m found by the linear regression of the FE analyses (i.e., the values indicated with red squares in Fig. 16 (b)), and the dash-dotted lines if m is chosen according to Equation (23).

7.3. Model application

To assess the influence of the triaxial stress state on the force-elongation behaviour of a damaged reinforcing bar, the SLM (Equation (6)) is enhanced with (i) the increased apparent uniaxial tensile strength and (ii) the equivalent cross-sectional areas of the bar sections above and below the cross-section transition, see Fig. 17.

The material stress–strain relationship ε_s-σ_s (e.g. from a conventional tensile test, black curve in Fig. 17) is converted into the relationship $\varepsilon_{s,triax}$-$\sigma_{s,triax}$ accounting for strain localisation and the triaxial stresses, which applies for the bar over a length $L_{tot} = L_c + 2\varnothing$. For $\varnothing = 18$ mm, $\varnothing_c = 17$ mm, and $L_c = 10$ mm, the blue solid line results according to the SLM in Equation (6), exhibiting severe strain localisation mainly due to the reduced strain outside the pit (dashed blue line). The red solid line results from the simplified modelling approach, described in the following, and applying the model parameters p_σ, $p_{\varepsilon,c}$, and $p_{\varepsilon,uc}$ to account for the effects of the triaxial stress state.

1. Estimate the fitting parameters a, b, m using Equations (20), (21), and (23), depending on the steel type, with $c = 1.0$ (CW) or $c = 1.01$ (QST).
2. Use Equations (19) and (22) to determine the parameters p_σ, $p_{\varepsilon,c}$, and $p_{\varepsilon,uc}$.

3. Determine the vector of apparent uniaxial stress $\sigma_{s,triax}$, and the auxiliary stress vectors $\overline{\sigma_{s,c}}$ and $\overline{\sigma_{s,uc}}$:

$$\begin{aligned}\sigma_{s,triax} &= p_\sigma \sigma_s \\ \overline{\sigma_{s,c}} &= \frac{\sigma_{s,triax}}{p_{\varepsilon,c}} = \frac{p_\sigma}{p_{\varepsilon,c}}\sigma_s \\ \overline{\sigma_{s,uc}} &= \frac{\sigma_{s,triax}A_{s,c}}{p_{\varepsilon,uc}A_s} = \frac{p_\sigma}{p_{\varepsilon,uc}}\frac{A_{s,c}}{A_s}\sigma_s\end{aligned} \tag{24}$$

4. Obtain the strain vectors $\varepsilon_{s,c}$, $\overline{\varepsilon_{s,c}}$, $\overline{\varepsilon_{s,uc}}$, corresponding to the stresses determined in Step 3 from the material stress–strain curve

$$\begin{aligned}\varepsilon_{s,c} &= \begin{cases} \varepsilon_s(\sigma_{s,triax}) & \text{if } \sigma_{s,triax} \leqslant f_{su} \\ A_{gt} & \text{if } \sigma_{s,triax} > f_{su} \end{cases} \\ \overline{\varepsilon_{s,c}} &= \begin{cases} \varepsilon_s(\overline{\sigma_{s,c}}) & \text{if } \overline{\sigma_{s,c}} \leqslant f_{su} \\ A_{gt} & \text{if } \overline{\sigma_{s,c}} > f_{su} \end{cases} \\ \overline{\varepsilon_{s,uc}} &= \begin{cases} \varepsilon_s(\overline{\sigma_{s,uc}}) & \text{if } \overline{\sigma_{s,uc}} \leqslant f_{su} \\ A_{gt} & \text{if } \overline{\sigma_{s,uc}} > f_{su} \end{cases}\end{aligned} \tag{25}$$

5. Determine the strain vector ε_s' by weighting and summing up the strains of Step 4

$$\begin{aligned}\varepsilon_{s,triax} &= \frac{(L_c - 2\varnothing_c)\varepsilon_{s,c} + 2\varnothing_c\overline{\varepsilon_{s,c}} + 2\varnothing\overline{\varepsilon_{s,uc}}}{L_{tot}} && \text{for } L_c > 2\varnothing_c \\ \varepsilon_{s,triax} &= \frac{L_c\overline{\varepsilon_{s,c}} + 2\varnothing\overline{\varepsilon_{s,uc}}}{L_{tot}} && \text{for } L_c \leqslant 2\varnothing_c\end{aligned} \tag{26}$$

Note the similarity of Equations (26) and (6). Inserting the stress $\sigma_{s,c} = F/A_{s,c}$ (Equation (1)) in the $\varepsilon_{s,triax}$-$\sigma_{s,triax}$ relationship yields the mean strain exhibited by the bar section with length L_{tot}, accounting for the effects of the triaxial stress state. Failure of the bar at the pit occurs, if $\sigma_{s,c} = p_\sigma f_{su}$.

7.4. Model evaluation

Fig. 18 (a, b) (CW bars) and (d, e) (QST bars) show the deviation in the strain at peak stress of the simplified model from the FE analyses, similar to the comparison between FE analyses and the SLM illustrated in Fig. 12. The black lines correspond to constant normalised damage lengths, and circles indicate the maximum and minimum ratios found in the parameter range.

Fig. 18 (a) and (d) show the results obtained using the individual regression parameters of each FE analysis for evaluating Equations (19) and (22), while Fig. 18 (b) and (e) are based on the regression parameters approximated with Equations (20), (21), and (23). In the former case, the strain at peak stress is slightly underestimated; in the latter case, deviations are generally higher (as expected, since two regression steps are now included), and the strain at peak stress is more pronouncedly underestimated for very short damage lengths $L_c/(2\varnothing_c) = 0.2...0.3$. However, the deviations are still much smaller than those of the SLM neglecting the effects of the triaxial stress state, see Fig. 12.

Fig. 18 (c) and (f) show the stress–strain curves of the FE analyses, the SLM, and the simplified model with original and approximated model parameters for the four coloured target markers included in Fig. 18 (a, b, d, e), i.e., for the combinations $\zeta = 0.15,\ 0.4$ and $L_c/(2\varnothing_c) = 0.4,\ 0.8$. It is observed that the stress–strain curves of the FE analyses and both simplified models are virtually identical, whereas the curve based on the SLM underestimates the peak load and the strain at peak stress, particularly for shorter damage lengths.

The presented simplified model thus appears to reasonably capture the altered stress–strain behaviour of bars containing a axisymmetric corrosion damage, accounting for both strain localisation as well as the effect of triaxial stresses near the cross-section transition. However, it needs to be validated in a larger experimental campaign for different material behaviour and a wider range of geometrical parameters, and extended to non-axisymmetric damage in future studies.

8. Summary and conclusions

Numerous experimental campaigns aiming to characterise the stress–strain behaviour of reinforcing bars affected by local corrosion have been conducted to date, using both naturally corroded and artificially damaged bars. However, the behaviour has been described mainly empirically, and only few researchers tried to derive mechanically consistent models. However, such models are essential to understand and describe the various effects caused by local corrosion damages.

This paper investigated the influence of a triaxial stress state on the stress–strain behaviour of reinforcing bars affected by local corrosion, focusing on axisymmetric damage. It was found that the triaxial stress state inside and near the damage zone of a corroded bar strongly influences the apparent uniaxial stress–strain behaviour, typically enhancing the tensile strength and deformation capacity, which explains experimental observations that cannot be attributed to strain localisation alone. Likewise strain localisation, the triaxial stress state is mainly governed by the material characteristics, especially in the inelastic phase, and the geometrical characteristics of the damage. Therefore, if local corrosion is considered, it is all the less expedient to describe damage of a bar merely by its mass loss, as it is still common practice in many experimental campaigns despite having been criticised in former studies [5,6,48]. An effort should therefore be made to a better characterisation of the corrosion damage geometry and its mechanical influence on the apparent uniaxial stress–strain behaviour of affected bars, as previously suggested by other researchers [1,4,6].

The following findings emerged from experiments and theoretical considerations of this study:

- Due to the local deviation of the stress trajectories, a triaxial stress state occurs inside and near the damage zone of reinforcing bars affected by local corrosion. The significant radial, tangential and shear stresses present in the vicinity of the cross-section transition change the local steel stress–strain behaviour, particularly for short damage lengths.
- For axisymmetric damage, the triaxial stress state mainly depends on the shape of the steel stress–strain curve in the inelastic phase, the damage length and the cross-section reduction. Its effects are most pronounced for severe cross-section losses and short damage lengths. For damage lengths exceeding twice the residual diameter, the influence of the triaxial stresses on the apparent uniaxial peak stress and deformation capacity is negligible.
- For short damage lengths, the triaxial stress state leads to a considerable increase of the apparent uniaxial peak stress, which can be up to 35% higher than the uniaxial tensile strength for high cross-section losses, with experimental evidence of up to 4% higher peak stresses even for slight cross-section losses of merely 10 to 15%. Similar experimental findings were reported in previous studies [1,14,23,24], and are mechanically substantiated by this study.
- Experimental observations show that the tensile stiffness of a bar is reduced in the undamaged part near the cross-section transition, but

increased in the adjoining parts of the damage zone. This is explained by the radial and tangential compressive and tensile stresses acting on the undamaged and damaged side of the cross-section transition, respectively. The length over which the altered behaviour is observed comprises approximately one bar diameter.

- The triaxial stress state was found to alter the yield behaviour near the corrosion damage of reinforcing steels exhibiting a yield plateau, as previously reported by [23]. The yield plateau (due to the propagation of Lüders bands) is lost, and strain hardening directly follows the elastic phase. The loss of the yield plateau might be caused by the rotating principal directions as direct consequence of the deviated stress trajectories, preventing the of Lüders bands to progress.
- The lower stiffness and reduced yield strength in front of the damage zone, combined with the higher peak stress, can lead to a significantly higher deformation capacity of damaged bars than would be assumed by established concepts of strain localisation. This particularly applies to short damage lengths and small to moderate cross-section losses below 15…20%.
- While the triaxial stress state was investigated with a nonlinear FE model considering von Mises / J_2-plasticity in this study, such a model is deemed inadequate for application to entire structures due to its high computational cost. Hence, a simplified modelling approach is proposed to estimate the combined influence of strain localisation and the triaxial stress state on the stress–strain behaviour of damaged reinforcing bars.
- The simplified modelling approach correlates well with the FE analyses carried out in this study. However, it is restricted to axisymmetric damage and needs to be validated in a larger experimental campaign regarding different material characteristics and damage geometries.
- The application range of this study is limited to axisymmetric local damage of reinforcing bars, and the results may not directly apply to bars exhibiting unilateral corrosion damage. It was shown that unilateral damages additionally cause bending stresses in the pit vicinity [2,12], which may soften the stress–strain behaviour in this part of the bar (yield stress is reached at lower load), but may also reduce the failure load.

The increased peak load and especially the increased deformation at peak load imply that load redistributions between locally corroding and uncorroded reinforcing bars inside a structure might be possible to a larger extent than what has been assumed up to now. A recent study [49] applying the findings presented in this paper in the analysis of experimental results on corroded retaining wall segments [12] concluded that such load redistributions directly cohere to the effects of the triaxial stress state at the corrosion pits. Corroding structures might thus exhibit a higher resilience than considered today and their service life might be prolonged. However, more research is needed regarding the influence of the pit geometry (especially for non-axisymmetric damage) to further substantiate this hypothesis.

9. Notation

$A_{gt} = \varepsilon\left(f_{su,dyn}\right)$	Strain at steel tensile strength
A_s, $A_{s,c}$	Reinforcing bar cross-sectional area (initial, reduced)
A_s^{eq}, $A_{s,c}^{eq}$	Equivalent cross-sectional areas in (undamaged, damaged) section, for simplified modelling approach
a	Fitting parameter
b, b_1, b_2	Fitting parameters
c	Rib distance, fitting parameter
c_1, c_2, c_3, c_4	Coefficients for steel constitutive relationship
E_s	Young's modulus of reinforcing steel
F, F_u	Axial normal force (in general, maximum)
f_{sy}, $f_{sy,dyn}$	Steel yield stress (in general, dynamic value)
f_{su}, $f_{su,dyn}$	Steel tensile strength (in general, dynamic)
K	Coefficient for steel constitutive relationship
L_{tot}, L_c, L_{uc}	Total bar length, length of damaged section, length of section with initial diameter (undamaged)
m	Fitting parameter
p_σ, $p_{\varepsilon,c}$, $p_{\varepsilon,uc}$	Parameters to simplified modelling approach to account for the influence of the triaxial stresses on the apparent uniaxial stress and the axial strains
r, R	Distance from bar centre, outermost radius ($R = \varnothing/2$)
x, x', x_1, x_2	Coordinates (parallel to bar axis), with $x' = x - L_c/2$
$\varepsilon_{s,eng}$, $\varepsilon_{s,tr}$	Steel strain (engineering, true, with $\varepsilon_{s,tr} = \ln(1+\varepsilon_{s,eng})$)
ε_s, $\varepsilon_{s,c}$, $\varepsilon_{s,uc}$	Steel strain in general, steel strain in section with (reduced, initial) cross-sectional area
$\varepsilon_{s,h}$	Steel strain at hardening
$\varepsilon_{s,m}$, $\varepsilon_{s,m}^{SLM}$	Mean strain over total bar length (measured, or according to strain localisation model (SLM))
$\overline{\varepsilon_s}$, $\overline{\varepsilon_{uc}}$	Mean strain over $1\varnothing_c$ of damaged zone, and over $1\varnothing$of adjacent undamaged section, respectively, for simplified modelling approach
$\sigma_{s,eng}$, $\sigma_{s,tr}$	Steel stress (engineering, true, with $\sigma_{s,tr} = \sigma_{s,eng}(1+\varepsilon_{s,eng})$)
σ_s, $\sigma_{s,c}$, $\sigma_{s,uc}$	Steel stress in general, steel stress referred to (reduced, initial) cross-sectional area
$\sigma_{s,c,max}$, $\sigma_{s,uc,max}$	Steel stress at maximum load referred to (reduced, initial) cross-sectional area
σ_{vM}, $\overline{\sigma_{vM}}$	Von Mises stress (in general, mean over cross-section)
σ_x, $\overline{\sigma_x}$, σ_r, σ_φ	Axial stress (in general, mean over cross-section), radial, and tangential stress
τ_{rx}, $\tau_{r\varphi}$, $\tau_{x\varphi}$	Shear stresses
ζ, ζ_{crit}	Relative cross-section loss of reinforcing bar (in general, critical)
ζ_{mart}, ζ_{bain}	Relative cross-section loss of reinforcing bar for which (martensitic, bainitic) microstructure layer is lost
$\varnothing$, $\varnothing_c$	Reinforcing bar diameter (initial, reduced)

CRediT authorship contribution statement

Severin Haefliger: Conceptualization, Methodology, Software, Validation, Formal analysis, Investigation, Writing – original draft, Visualization. **Karel Thoma:** Conceptualization, Methodology, Software, Writing – review & editing. **Walter Kaufmann:** Conceptualization, Writing – review & editing, Supervision, Funding acquisition.

Declaration of Competing Interest

The authors declare that they have no known competing financial interests or personal relationships that could have appeared to influence the work reported in this paper.

Data availability

Data will be made available on request.

Acknowledgements

The authors gratefully acknowledge the support of Sara Fomasi, who contributed in conducting the experiments as part of her Master's Thesis. The support of the team of the structures laboratory, especially of Dominik Werne, Christoph Gisler, Pius Herzog, and Thomas Jaggi, is greatly acknowledged. This study was partially funded by the Swiss Federal Roads Office and the Swiss Federal Office of Transport (Project AGB 2015/028).

Appendix

Fig. A1

References

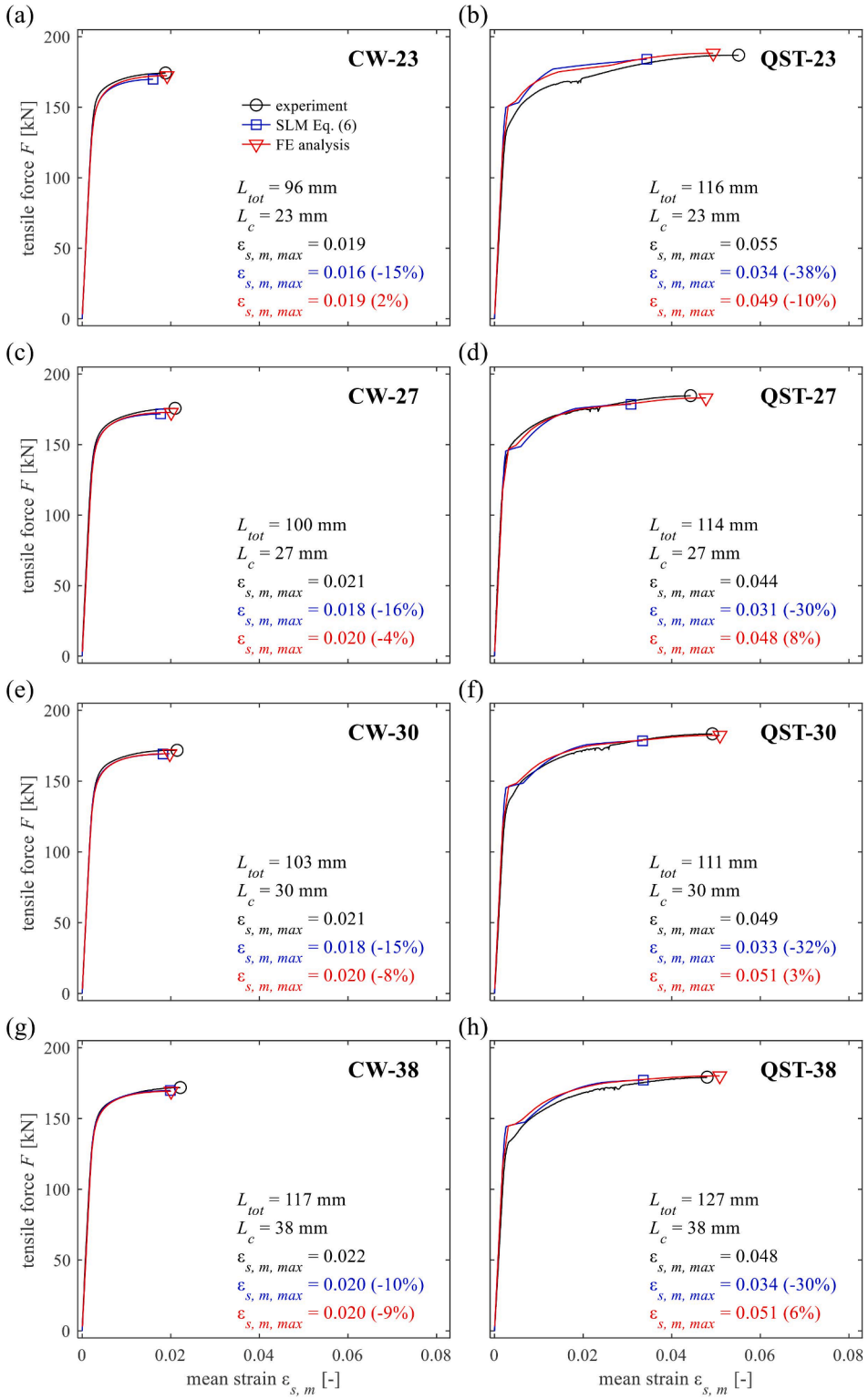

Fig. A1. Comparison of experimental results (black) with the SLM (Equation (6), blue) and the FE analyses (red): (a,c,e,g) Series CW; (b,d,f, h) Series QST; specimens with damage lengths L_c = 23, 27, 30, and 38 mm. The markers indicate the peak loads. Additionally, the total gauge length L_{tot} and the mean strain at peak load $\varepsilon_{s,m,max}$ are reported, as well as the relative deviation between the models and the experimental result. (For interpretation of the references to colour in this figure legend, the reader is referred to the web version of this article.)

[1] E. Chen, C.G. Berrocal, I. Fernandez, I. Löfgren, K. Lundgren, Assessment of the mechanical behaviour of reinforcement bars with localised pitting corrosion by Digital Image Correlation, Eng. Struct. 219 (2020), 110936, https://doi.org/10.1016/j.engstruct.2020.110936.

[2] K. Andisheh, A. Scott, A. Palermo, Modeling the influence of pitting corrosion on the mechanical properties of steel reinforcement, Mater. Corros. 67 (2016) 1220–1234, https://doi.org/10.1002/maco.201508795.

[3] C.A. Apostolopoulos, S. Demis, V.G. Papadakis, Chloride-induced corrosion of steel reinforcement – Mechanical performance and pit depth analysis, Constr. Build. Mater. 38 (2013) 139–146, https://doi.org/10.1016/j.conbuildmat.2012.07.087.

[4] W. Zhu, R. François, C.S. Poon, J.-G. Dai, Influences of corrosion degree and corrosion morphology on the ductility of steel reinforcement, Constr. Build. Mater. 148 (2017) 297–306, https://doi.org/10.1016/j.conbuildmat.2017.05.079.

[5] R. Hingorani, F. Pérez, J. Sánchez, J. Fullea, C. Andrade, P. Tanner. Loss of ductility and strength of reinforcing steel due to pitting corrosion, presented at the VIII International Conference on Fracture Mechanics of Concrete and Concrete Structures FraMCoS-8, Toledo, 2013.

[6] I. Finozzi, A. Saetta, H. Budelmann, Structural response of reinforcing bars affected by pitting corrosion: experimental evaluation, Constr. Build. Mater. 192 (2018) 478–488, https://doi.org/10.1016/j.conbuildmat.2018.10.088.

[7] M.M. Kashani, A.J. Crewe, N.A. Alexander, Nonlinear stress–strain behaviour of corrosion-damaged reinforcing bars including inelastic buckling, Eng. Struct. 48 (2013) 417–429, https://doi.org/10.1016/j.engstruct.2012.09.034.

[8] S. Imperatore, Z. Rinaldi, Mechanical behaviour of corroded rebars and influence on the structural response of R/C elements, in: Concrete Repair, Rehabilitation and Retrofitting II, Taylor & Francis, London, 2009, pp. 489–495.

[9] R. Palsson, M.S. Mirza, Mechanical response of corroded steel reinforcement of abandoned concrete bridge, ACI Struct. J. 99 (2002) 157–162. https://doi.org/10.14359/11538.

[10] J. Cairns, G.A. Plizzari, Y. Du, D.W. Law, C. Franzoni, Mechanical properties of corrosion-damaged reinforcement, ACI Materials J. 102 (4) (2005) 256–264.

[11] C. Zeng, J.-H. Zhu, C. Xiong, Y. Li, D. Li, J. Walraven, Analytical model for the prediction of the tensile behaviour of corroded steel bars, Constr. Build. Mater. 258 (2020), 120290, https://doi.org/10.1016/j.conbuildmat.2020.120290.

[12] S. Haefliger, W. Kaufmann, Load-deformation behavior of locally corroded reinforced concrete retaining wall segments: Experimental results, Struct. Concr. 24 (1) (2023) 288–317, https://doi.org/10.1002/suco.202200405.

[13] S. Haefliger, W. Kaufmann, Corroded Tension Chord Model: Load-deformation behavior of structures with locally corroded reinforcement, Struct. Concr. 23 (1) (2022) 104–120, https://doi.org/10.1002/suco.202100165.

[14] S. Imperatore, Mechanical Properties Decay of Corroded Reinforcement in Concrete—An Overview, Corros. Mater. Degrad. 3 (2022) 210–220, https://doi.org/10.3390/cmd3020012.

[15] P.D. Flynn, A.A. Roll, A re-examination of stresses in a tension bar with symmetrical U-shaped grooves, Exp. Mech. 6 (1966) 93–98, https://doi.org/10.1007/BF02326227.

[16] J.W. Hancock, A.C. Mackenzie, On the mechanisms of ductile failure in high-strength steels subjected to multi-axial stress-states, J. Mech. Phys. Solids. 24 (1976) 147–160, https://doi.org/10.1016/0022-5096(76)90024-7.

[17] T. Foecke, M.A. Iadicola, A. Lin, S.W. Banovic, A Method for Direct Measurement of Multiaxial Stress-Strain Curves in Sheet Metal, Metall. Mater. Trans. A. 38A (2007) 306–313, https://doi.org/10.1007/s11661-006-9044-y.

[18] W. Lode, Versuche über den Einfluß der mittleren Hauptspannung auf das Fließen der Metalle Eisen, Kupfer und Nickel, Zeitschrift für Physik 36 (1926) 913–939, https://doi.org/10.1007/BF01400222.

[19] M. Basaran, Stress state dependent damage modeling with a focus on the lode angle influence, in: Doctoral Dissertation, Institute of General Mechanics, RTWH Aachen, 2011.

[20] F.X.C. Andrade, M. Feucht, A. Haufe, F. Neukamm, An incremental stress state dependent damage model for ductile failure prediction, Int. J. Fract. 200 (2016) 127–150, https://doi.org/10.1007/s10704-016-0081-2.

[21] M. Murugesan, D. Jung, Johnson Cook Material and Failure Model Parameters Estimation of AISI-1045 Medium Carbon Steel for Metal Forming Applications, Materials. 12 (2019) 609, https://doi.org/10.3390/ma12040609.

[22] W.D. Pilkey, D.F. Pilkey, Peterson's Stress Concentration Factors, 3rd ed., John Wiley & Sons, New Jersey, 2008.

[23] R. François, I. Khan, V.H. Dang, Impact of corrosion on mechanical properties of steel embedded in 27-year-old corroded reinforced concrete beams, Mater. Struct. 46 (2013) 899–910, https://doi.org/10.1617/s11527-012-9941-z.

[24] F. Tang, Z. Lin, G. Chen, W. Yi, Three-dimensional corrosion pit measurement and statistical mechanical degradation analysis of deformed steel bars subjected to accelerated corrosion, Constr. Build. Mater. 70 (2014) 104–117, https://doi.org/10.1016/j.conbuildmat.2014.08.001.

[25] I. Fernandez, J.M. Bairán, A.R. Marí, 3D FEM model development from 3D optical measurement technique applied to corroded steel bars, Constr. Build. Mater. 124 (2016) 519–532, https://doi.org/10.1016/j.conbuildmat.2016.07.133.

[26] D. Russwurm, Betonstähle für den Stahlbetonbau, Bauverlag, Wiesbaden, Berlin, 1993.

[27] O. Keleştemur, M.H. Kelestemur, S. Yildiz, Improvement of mechanical properties of reinforcing steel used in the reinforced concrete structures, J. Iron Steel Res. Int. 16 (2009) 55–63, https://doi.org/10.1016/S1006-706X(09)60044-3.

[28] J.F. Noville, N. Jean-François, TEMPCORE®, the most convenient process to produce low cost high strength rebars from 8 to 75 mm, presented at the METEC & 2nd ESTAD European Steel Technology and Application Days, Düsseldorf, 2015.

[29] A. Ray, D. Mukerjee, S.K. Sen, A. Bhattacharya, S.K. Dhua, M.S. Prasad, N. Banerjee, A.M. Popli, A.K. Sahu, Microstructure and properties of thermomechanically strengthened reinforcement bars: a comparative assessment of plain-carbon and low-alloy steel grades, J. Mater. Eng. Perform. 6 (1997) 335–343, https://doi.org/10.1007/s11665-997-0098-9.

[30] G. Rehm, D. Russwurm, Assessment of Concrete Reinforcing Bars made by the Tempcore Process, Betonwerk + Fertigteiltechnik 6 (1977) 300–307.

[31] S. Haefliger, W. Kaufmann, Influence of cross section loss on the stress-strain characteristics of corroded quenched and self-tempered reinforcing bars, Constr. Build. Mater. 282 (2021), 122598, https://doi.org/10.1016/j.conbuildmat.2021.122598.

[32] B. Hortigón Fuentes, J.M. Gallardo Fuentes, P. Gümpel, J. Strittmacher, Wirkung der Tempcore-Behandlung auf die Zugeigenschaften von Stabstahl, Stahl Eisen. 138 (2018) 45–52.

[33] J. Santos, A.A. Henriques, Strength and Ductility of Damaged Tempcore Rebars, Procedia Eng. 114 (2015) 800–807, https://doi.org/10.1016/j.proeng.2015.08.029.

[34] C. Apostolopoulos, A. Drakakaki, A. Apostolopoulos, T. Matikas, A.I. Rudskoi, G. Kodzhaspirov, Characteristic defects-corrosion damage and mechanical behaviour of dual phase rebar, Mater. Phys. Mech. 30 (2017) 19.

[35] Ch.Alk. Apostolopoulos, G. Diamantogiannis, Alk.Ch. Apostolopoulos, Assessment of the Mechanical Behavior in Dual-Phase Steel B400C, B450C, and B500B in a Marine Environment, J. Mater. Civ. Eng. 28 (2016) 04015097, https://doi.org/10.1061/(ASCE)MT.1943-5533.0001271.

[36] FEDRO, Evaluation de l'état des murs de soutènement béton à semelle. Etude pilote. Rapport de synthèse des phases 1 et 2., UVEK, Swiss Federal Roads Office FEDRO, 2014.

[37] S. Haefliger, S. Fomasi, W. Kaufmann, Influence of quasi-static strain rate on the stress-strain characteristics of modern reinforcing bars, Constr. Build. Mater. 287 (2021) 7, https://doi.org/10.1016/j.conbuildmat.2021.122967.

[38] W. Ramberg, W.R. Osgood, Description of stress–strain curves by three parameters, National Advisory Committee For Aeronautics, Washington DC., 1943.

[39] T. Galkovski, Y. Lemcherreq, J. Mata-Falcón, W. Kaufmann, Fundamental Studies on the Use of Distributed Fibre Optical Sensing on Concrete and Reinforcing Bars, Sensors. 21 (2021) 7643, https://doi.org/10.3390/s21227643.

[40] Y. Lemcherreq, T. Galkovski, J. Mata-Falcón, W. Kaufmann, Application of Distributed Fibre Optical Sensing in Reinforced Concrete Elements Subjected to Monotonic and Cyclic Loading, Sensors. 22 (2022) 2023, https://doi.org/10.3390/s22052023.

[41] J. Rösler, H. Harders, M. Bäker, Mechanisches Verhalten der Werkstoffe, 3rd ed., Vieweg + Teubner, Wiesbaden, 2008.

[42] J. Zhang, Y. Jiang, Lüders bands propagation of 1045 steel under multiaxial stress state, Int. J. Plast. 21 (2005) 651–670, https://doi.org/10.1016/j.ijplas.2004.05.001.

[43] K.-A Reckling, in: ‚Plastizitätstheorie und Ihre Anwendung auf Festigkeitsprobleme, Springer, Berlin, Heidelberg, 1967.

[44] R.W.K. Honeycombe, The Plastic Deformation of Metals, Second Edition, Edward Arnold, London, 1984.

[45] A.H. Cottrell, B.A. Bilby, Dislocation Theory of Yielding and Strain Ageing of Iron, Proc. Phys. Soc. Sect. A. 62 (1949) 49–62, https://doi.org/10.1088/0370-1298/62/1/308.

[46] D.E. Delwiche, D.W. Moon, Orientation of Lüders Band Fronts, Mater. Sci. Eng. 7 (1971) 203–207, https://doi.org/10.1016/0025-5416(71)90146-7.

[47] Y. Lemcherreq, S. Haefliger, W. Kaufmann, Discontinuous yielding in bare and embedded reinforcing bars: implications on the determination of steel and bond shear stresses from strain measurements, Eng. Struct. 278 (2023), 115235, https://doi.org/10.1016/j.engstruct.2022.115235.

[48] D. Li, R. Wei, L. Li, X. Guan, X. Mi, Pitting corrosion of reinforcing steel bars in chloride contaminated concrete, Constr. Build. Mater. 199 (2019) 359–368, https://doi.org/10.1016/j.conbuildmat.2018.12.003.

[49] S. Haefliger, Load-deformation behaviour of reinforced concrete structures affected by local corrosion, Doctoral dissertation no. 29029, Institute of Structural Engineering, ETH Zurich (2023), https://doi.org/10.3929/ethz-b-000602335.